Resonance Raman and surface- and tip-enhanced Raman spectroscopy methods to study solid catalysts and heterogeneous catalytic reactions†

Hacksung Kim,*[ab] Kathryn M. Kosuda,[a] Richard P. Van Duyne[a] and Peter C. Stair*[ab]

Received 16th July 2010
DOI: 10.1039/c0cs00044b

Resonance Raman (RR) spectroscopy has several advantages over the normal Raman spectroscopy (RS) widely used for *in situ* characterization of solid catalysts and catalytic reactions. Compared with RS, RR can provide much higher sensitivity and selectivity in detecting catalytically-significant surface metal oxides. RR can potentially give useful information on the nature of excited states relevant to photocatalysis and on the anharmonic potential of the ground state. In this *critical review* a detailed discussion is presented on several types of RR experimental systems, three distinct sources of so-called Raman (fluorescence) background, detection limits for RR compared to other techniques (EXAFS, PM-IRAS, SFG), and three well-known methods to assign UV-vis absorption bands and a band-specific unified method that is derived mainly from RR results. In addition, the virtues and challenges of surface-enhanced Raman spectroscopy (SERS) are discussed for detecting molecular adsorbates at catalytically relevant interfaces. Tip-enhanced Raman spectroscopy (TERS), which is a combination of SERS and near-field scanning probe microscopy and has the capability of probing molecular adsorbates at specific catalytic sites with an enormous surface sensitivity and nanometre spatial resolution, is also reviewed (300 references).

1. Introduction

Vibrational spectroscopy has been extensively applied to study gas, liquid, and solid materials in a wide variety of fields of chemical sciences. It generally provides more and better-resolved bands and thus contains more information than UV to near IR electronic spectroscopy. Compared with IR (absorption, reflection, reflection-absorption) spectroscopy, electron energy loss spectroscopy, and sum frequency generation vibrational spectroscopy, Raman spectroscopy (RS) has advantages in probing solid catalysts and reagents under working conditions of high temperature and pressure and in the low frequency region, $< \sim 1100\ cm^{-1}$, where vibrational bands in solid catalysts appear.

Like other spectroscopic techniques, RS also has some drawbacks, which limit its usefulness. In the field of heterogeneous

[a] *Department of Chemistry, Center for Catalysis and Surface Science, and Institute for Catalysis and Energy Processes, Northwestern University, Evanston, Illinois 60208, USA. E-mail: hskim@northwestern.edu, pstair@northwestern.edu*
[b] *Chemical Sciences and Engineering Division, Argonne National Laboratory, Argonne, Illinois 60439, USA*
† Part of the themed issue covering recent advances in the *in situ* characterization of heterogeneous catalysts.

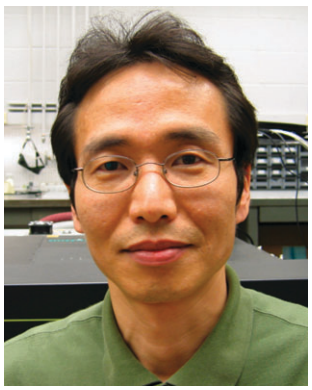

Hacksung Kim

Hacksung Kim is Research Associate Professor in the Center for Catalysis and Surface Science at Northwestern University and Raman lab Supervisor in the Chemical Sciences and Engineering Division at Argonne National Laboratory. His current research focuses on the application of resonance Raman spectroscopy to in situ characterization of solid catalysts and materials. Before joining Northwestern/Argonne, he studied unidentified IR emission bands in the field of molecular astrophysics and astrochemistry as a postdoctoral fellow at the University of California, Berkeley after receiving a PhD in Physical Chemistry for studies in cryogenic vibrational spectroscopy from Seoul National University.

Kathryn M. Kosuda

Kathryn M. Kosuda is from the suburbs of New York City. She received her BA in chemistry from Colby College in Waterville, Maine, USA. She is currently a PhD candidate in chemistry at Northwestern University, co-advised by Prof. Peter Stair and Prof. Richard Van Duyne. Her research focuses on the use of atomic layer deposition for applications in plasmonics and catalysis.

catalysis, the drawbacks have been summarized in several reviews[2–4] and include (1) strong background emission due to fluorescence which makes Raman bands weak or completely undetectable, (2) the intrinsic low sensitivity of RS particularly at low loadings of active material, and (3) the possibility of sample degradation induced by the excitation laser (especially in the UV). All three drawbacks occur not only in many solid catalysts, but also in other liquid and solid materials and are intrinsic to Raman. The last issue depends on the (optical and thermal) properties of the materials, the residence time in the laser beam, the excitation wavelength, and power density of the laser. However, even under very problematic situations (*e.g.*, deep UV excitation combined with photosensitive adsorbates on a catalytic surface), this problem has been successfully overcome by the fluidized bed technique developed by Chua and Stair.[5,6]

Problem (1) occurs in many catalytic and chemical systems, but can be avoided by UV excitation or time-gating methods. This problem is discussed in some detail in this review. Since the early Raman studies of oxide materials, the background has been attributed to fluorescence that originates from a variety of sources, but there are also non-fluorophore and non-fluorescence sources. These sources are associated with the presence of defect sites and surface hydroxyl groups of high surface area metal oxides, respectively. In this review, three distinct sources are identified, fluorophores, defects, and strong anharmonic interactions, that can simultaneously contribute to the Raman background.

Problem (2) also occurs in many catalytic systems, but can be mitigated by resonance Raman (RR) spectroscopy. A detailed comparison of the RR detection sensitivity with other techniques is provided. In situations where sensitivity is poor due to very small concentrations of molecular adsorbates, surface-enhanced and tip-enhanced Raman spectroscopy (SERS and TERS) can be exploited to achieve superior surface sensitivity. This review also describes the applications of SERS and TERS to catalytically relevant conditions.

We provide a perspective on the advantages of RR spectroscopy compared to nonresonance RS. For example, RR can confirm previous assignments of UV-vis absorption bands while providing additional detail. Several types of RR instruments are described in order to assist in the selection of an appropriate RR system tailored to research requirements.

Before beginning the main topics, we briefly review the two main RR theories, an empirical RR rule, and the early application of RR and UV Raman spectroscopy in the field of heterogeneous catalysis.

Early applications of RR or UV Raman to heterogeneous catalysts

UV-visible RR spectroscopy studies of molecular species adsorbed on catalytic oxide supports were first reported in the 70's. Nagasao and Yamada[7] in 1975 reported overtone Raman bands (up to 4th order for totally symmetric I–I stretch) of I_2 adsorbed on silica using 488 nm excitation. The same group, Yamada and Yamamoto,[8] in the late 70's reported intensified Raman bands of pyridine adsorbed on porous Vycor glass and on alumina with 364 nm UV excitation. They compared their UV and visible Raman results with spectra obtained in several liquid solutions. Interestingly, the UV Raman bands for two totally symmetric pyridine stretches (CH and ring) were enhanced by 3–60 times, depending on the solvent, when compared to the visible Raman data.

The first direct detection of surface (transition) metal oxide species by UVRR was reported in 1994 by Smudde and Stair.[9] They observed a new (enhanced) band at 935 cm^{-1} with 351 nm UV excitation that was not detectable with 514.5 nm visible excitation. The band was assigned to the MoO stretching vibrations of surface molybdenum oxide species. A similar enhancement of the MoO stretching band has been reported by Xiong *et al.*[10] for $Mo/\gamma\text{-}Al_2O_3$. The MoO stretching band at 910 cm^{-1} was enhanced strongly and moderately with 244 nm and 325 nm excitations, respectively.

Richard P. Van Duyne

Richard P. Van Duyne is Charles E. and Emma H. Morrison Professor of Chemistry at Northwestern University and is a member of the National Academy of Sciences. He received his PhD from the University of North Carolina at Chapel Hill. His research interests include surface-enhanced Raman spectroscopy, nanosphere lithography, localized surface plasmon resonance spectroscopy, molecular plasmonics, chemical and biological sensing, structure and function of biomolecules on surfaces, tip-enhanced Raman spectroscopy, ultrahigh vacuum scanning tunneling microscopy, ultrahigh vacuum surface science, Raman spectroscopy of mass-selected clusters, and application of surface-enhanced Raman spectroscopy to the study of works of art.

Peter C. Stair

Peter C. Stair is Professor of Chemistry, Director of the Center for Catalysis and Surface Science and of the Institute for Catalysis in Energy Processes at Northwestern University. He is also a Senior Scientist in the Chemical Sciences and Engineering Division at Argonne National Laboratory and Deputy Director of the Institute for Atom-efficient Chemical Transformations. He received a PhD in Chemistry from the University of California, Berkeley. His research interests are in the synthesis, characterization, and physical properties of heterogeneous catalysts with the objective of advancing catalysis science for industrial chemistry and energy technology.

2. Theory of resonance Raman (RR) scattering

A detailed description of RR scattering theory is available in a book[11] and several reviews.[12–18] Historical advances in RR theory have also been summarized.[16,17] What follows is a brief description of the theory without complicated theoretical equations and an empirical (Tsuboi) rule.

2.1 Sum-over-states formulation

In Raman scattering, the incident laser light induces a polarization in the sample whose direction and magnitude is described by a polarizability tensor with nine elements (six elements if the tensor is symmetric) designated xx, xy, xz, ..., zz. In the sum-over-states picture Raman scattering is considered as a two-photon process from an initial to a final state of the system, in which transition moments from the initial to various intermediate states, and from the intermediate states to the final state are involved. This process was initially expressed by Kramers–Heisenberg (KH) or Kramers–Heisenberg–Dirac (KHD) equations, where the elements of the Raman polarizability which contribute to a particular transition are related to sums over the vibrational (and rotational) states of all electric-dipole-allowed intermediate electronic states. Classical polarizability theory combined with molecular symmetry (point group theory) predicts which vibrational modes are Raman active, but cannot account for intensities and selective resonance enhancements.

Albrecht[19] derived a more quantitative theory of RR scattering by introducing the Herzberg–Teller expansion into the KH dispersion equation. Modern theory of RR intensities is mainly based on the work of Albrecht and collaborators,[19–21] who treated RR as a vibronic (vibrational and electronic) spectroscopy. In normal Raman scattering, the excitation does not interact with the excited electronic states and the polarizabilities (and polarizability derivatives) can be considered properties of the electronic ground state. In contrast, for RR scattering the incident laser frequency is resonant with one or more allowed electronic transitions. The positions of RR bands occur at electronic ground-state vibrational frequencies, but the intensities of RR bands include specific information on the structure and dynamics of the resonant electronic state.[14,22,23] Albrecht and collaborators[19–21] showed how RR intensity can arise from several mechanisms designated A-term (Franck–Condon overlap), B-term (Herzberg–Teller vibronic coupling), *etc*.

The A-term is associated with the Franck–Condon (F–C) approximation which is based on the Born–Oppenheimer (B–O) adiabatic approximation that is valid simply because a nucleus is much heavier than an electron. Under the F–C approximation, the electronic transition occurs vertically, *i.e*., without change in the nuclear positions in the molecule. Quantum mechanically, the intensity of a vibronic transition is proportional to the square of the overlap integral (F–C factor) between the vibrational wavefunctions of the ground and excited electronic states. B- and higher order terms are dependent on the interaction between electronic and nuclear motions.

For the A-term to be non-zero, two conditions must be met.[11,24,25] First, the transition dipole moment must be non-zero, *i.e*., the resonant electronic transition must be electric-dipole allowed. This requires the excitation wavelength to be within the contour of an intense charge transfer (CT) or π–π^* type absorption band. The RR intensity is proportional to the square of the absorption intensity.[26] Second, the vibrational overlap integral (F–C factor) must be non-zero. This condition is well-satisfied when there is a displacement of the potential energy minimum along the normal coordinate between the two (ground and excited) electronic states. Symmetry considerations require that such a displacement can occur only for totally symmetric modes unless the molecular symmetry changes in the excited state. With a small displacement only the fundamental vibration is enhanced. As the displacement increases, overtones (and combinations) are also observed, and their intensities increase relative to the intensity of the fundamental. Non-totally symmetric modes generally have no A-term contribution because there is no such displacement and do not show overtone progressions.[12] They can gain intensity in the fundamental with either A-term (*i.e*., F–C term *via* a change of symmetry or Jahn–Teller distortion in the resonant excited state) or B-term resonance scattering.[11,24]

The B-term is generally much smaller than the A-term,[11] and can play the dominant role only when the A-term is nearly zero. A-term and B-term enhancement can be differentiated using the observed UV-vis bands, RR excitation profiles (intensity of Raman bands as a function of the excitation wavelength), and a rapid decrease of Raman intensity that accompanies detuning from resonance.

2.2 Empirical Tsuboi rule and monomeric surface VO_4

Hirakawa and Tsuboi[27] formulated the following rule, called the Tsuboi rule, based on empirical observations of several molecules: "If a Raman band becomes stronger when the excitation frequency is brought closer to the frequency of an electronic band, then the equilibrium conformation of the molecule is distorted along the normal coordinate for the Raman band on going from the ground to the excited electronic state." The Tsuboi rule is valid for any totally symmetric, asymmetric, and degenerate Raman band.[26,28] They[27] illustrated the rule using the ammonia (NH_3) molecule. Ammonia is pyramidal in its ground state (X) and planar in its lowest excited electronic state (A, 217 nm above the ground state). On going from X to A states, the molecule should experience an umbrella motion. The Raman band at $\sim$950 cm^{-1} attributed to the umbrella vibration of the molecule is enhanced $\sim$10 times more than the symmetric stretching band near 3330 cm^{-1} when the excitation laser wavelength is changed from 514.5 nm to 351 nm.

Dehydrated monomeric vanadium oxide, O=V–$(OAl)_3$ can be considered as having pseudo C_{3v} (or C_s) point group symmetry[29] which is similar to the NH_3 structure. Unlike the gaseous NH_3 molecule, the presence of two or three V–O–Al linkages likely limits the umbrella motion with typical excitations of dehydrated surfaces. Three types of structural changes in the excited states can be inferred from the normal modes of O=V–$(OAl)_3$ (Fig. 1) and match well with a recent DFT molecular orbital calculation[30] for the C_{3v}

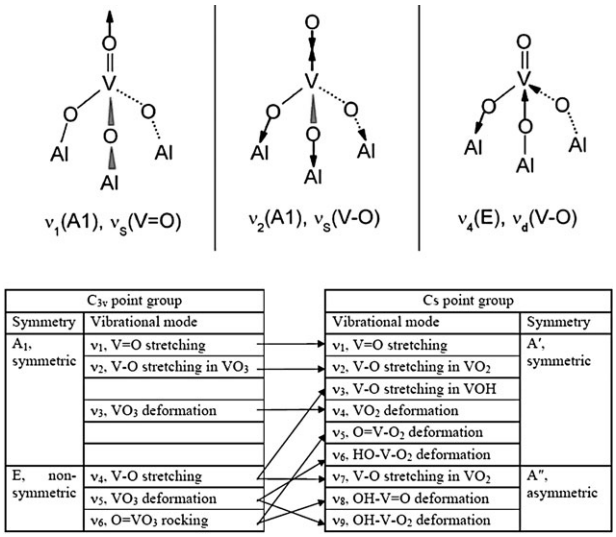

Fig. 1 VO_4-associated fundamentals in monomeric O═V(OH)$_x$(OAl)$_y$ (x = 0 and 1, y = 3 − x) structures belonging to the point groups of C_{3v} or C_s and their correlation. The Al-associated vibrations are not included. The degenerate 'E' mode of C_{3v} splits into one symmetric (A′) and one asymmetric (A″) mode of C_s. All fundamentals in C_{3v} and C_s are active both in the IR and Raman. Some approximate V–O stretching motions in C_{3v} symmetry are shown above. The subscripts 's' and 'd' denote symmetric- and degenerate-stretching vibrations, respectively. Table and drawing were taken from ref. 1.

structure: (1) totally-symmetric V═O stretching, (2) degenerate or symmetric and asymmetric V–O stretching, (3) VO_3 deformation and rocking. Totally-symmetric V═O stretching Raman bands near 1015 cm^{-1} were found[1] to be most strongly enhanced with 220 nm excitation. The Tsuboi rule suggests the axial V═O bond will be significantly elongated in its excited state (Fig. 2). Another distinct type of structural (Jahn–Teller) distortion was found[1] to exist with 287 nm excitation that is associated with the non-totally symmetric degenerate V–O stretching vibration.

2.3 Time-dependent formulation

The other major RR theory, designated as "time-dependent" theory, was initially developed by Lee and Heller *et al.*[31–33] In this picture, RR and Raman scattering (and optical absorption) can be described as the time integral of the overlap between (1) a propagating wave packet (given by the initial vibrational wavefunction times the transition dipole) on the Born–Oppenheimer surfaces under the influence of the excited state vibrational Hamiltonian and (2) the wavefunction of the final state in a Raman process (initial state in an optical absorption). At resonance the propagating wavepacket samples a larger portion of the surface than nonresonance. However, Raman scattering can be considered as a short time effect. Indeed, using the short time approximation, Heller[31,32] obtained a simple formula for the intensity ratio of the Raman fundamentals of two modes that is quite accurate in preresonance Raman spectra. He[31,32] also obtained a simple formula for the intensity ratio of the Raman overtone and fundamental bands. The formulae have been very useful for calculating excited state displacements.[34,35]

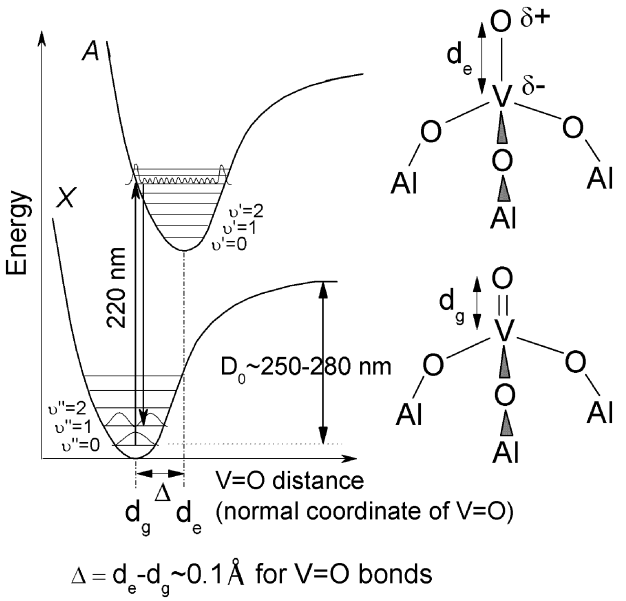

Fig. 2 Potential energy diagram for V═O vibrations in O═V–(OAl)$_3$. Vibronic vertical transition under Franck–Condon approximation and vibrational overlap are roughly illustrated. The 220 nm excitation corresponds to the charge transfer (from oxygen to vanadium) energy of V═O bonds. The selective enhancement of V═O Raman bands indicates the elongation of axial VO bonds in the excited state (Tsuboi rule). The X, A, υ'', υ', D_0 indicate the ground electronic state, an excited electronic state matching with 220 nm in energy, vibrational quantum numbers in the ground and excited electronic state, and dissociation energy, respectively. The values of Δ and D_0 for alumina supported vanadium oxides with different V concentration were taken from ref. 1.

This theory can be advantageous when the resonant electronic transition is very broad (due to either short lifetime or high density of allowed vibronic transitions) because the individual eigenstates are not resolved (and thus individual eigenvalues cannot be determined) in the classical KHD equation. Also, calculations for large molecules are typically more efficient using this theory.[16] On the other hand, calculated RR intensities using the short-time approximation can be overestimated due to strong dependence on the adjustable damping factor when compared to the results obtained using the vibronic theory.[36] Density Functional Theory can underestimate the RR intensities compared to the experimental results.[36] Nevertheless, RR spectra can be calculated accurately when the size of the system is not too large and the structure is known.[36]

3. Instrumentation for RR

3.1 Lasers for resonance Raman (RR) spectroscopy

The lasers employed to study solid catalysts and materials by RR spectroscopy will be reviewed.

3.1.1 Argon and Kr ion lasers for visible RR studies. In earlier resonance Raman (RR) studies of simple inorganic molecules and ions, discretely wavelength-tunable argon-ion (Ar^+) and krypton-ion (Kr^+) lasers have predominantly been used.[24] These lasers emit continuous wave (CW) output beams

at ~20 different wavelengths in the 407–676 nm visible region. The advantages of CW operation, the availability of many visible wavelengths in a single laser at wavelengths not covered by the frequency-doubled Ti:Sapphire laser, and ease of wavelength-tuning make these lasers useful for RR and SERS measurements.

3.1.2 First generation UV lasers for UVRR (UV resonance Raman) studies. RR studies of biological molecules commonly require UV lasers because their functional groups (chromophores) absorb in the UV. The development of UV laser systems for RR studies of organic[13] and biological[37,38] samples has been described in detail.[13,37,39,40] In brief, the first successful UV laser systems, that appeared[41–43] in the mid 80's, were nanosecond, pulsed, low duty cycle (10–20 Hz) Nd:YAG (neodymium-doped yttrium aluminium garnet, 1064 nm) lasers with high peak power. Continuous or discrete UV wavelengths were obtained by frequency doubling, tripling, or quadrupling and by application of a dye laser and/or a Raman shifter which shifts the incoming laser frequency by harmonics of the hydrogen stretching frequency of 4155 cm^{-1}. However, high peak power coupled to the low duty cycle could produce unwanted optical processes (*e.g.*, depletion of the ground state populations) and sample degradation or change during long data collection times.

3.1.3 Second generation UV lasers for UVRR studies. The second successful UV laser systems are characterized by intracavity frequency doubling of CW Ar^+ and Kr^+ lasers[44,45] with the BBO (β-BaB_2O_4) nonlinear optical crystal. The main advantages are higher signal-to-noise ratios, much lower peak powers due to CW operation, and simplified operation in comparison to Nd:YAG-based systems. The main disadvantage is a limited number of available UV wavelengths.

The helium–cadmium (HeCd) laser[46] (the first commercially available metal-vapor laser) is another CW UV excitation source and emits at 325 nm (also at 442 nm depending on the optics). 325 nm near-UV excitation by the HeCd laser[47–52] and the two 244 nm and 257 nm deep-UV excitations that are produced by frequency doubling the 488 nm and 514.5 nm lines of the Ar^+ laser, respectively,[52–55] have frequently been used in UV Raman studies of catalysts, materials, and biological samples.

3.1.4 Third generation UV-vis lasers for UV-vis RR studies. More advanced UV lasers for RR studies are characterized by quasi-CW (1–6 kHz repetition rate), pulsed (20–50 ns), all solid-state, continuously wavelength-tunable Ti:Sapphire-based laser systems.[39,40,56,57] The nanosecond pulse duration allows nanosecond time resolution in time-resolved resonance Raman (TR^3) or time-resolved temperature-jump UVRR measurements.[39,56,58] The "all solid-state" feature generally provides better stability and less electrical-power consumption. The laser peak power is low, but the average output power is sufficient for UVRR data acquisition. The laser line width is very narrow, <1 cm^{-1}, across the entire tuning range, which provides a narrow Raman band width and better discrimination of overlapping bands.

The Ti:Sapphire (Ti:Sa) laser is typically pumped by a Q-switched, intracavity, frequency-doubled Nd:YLF (yttrium lithium fluoride) laser emitting at 527 nm. It generates continuously tunable fundamental wavelengths in the ~770–920 nm region. Frequency doubling, tripling, and quadrupling of the Ti:Sa laser with LBO (LiB_3O_5) and BBO crystals generates continuously tunable wavelengths in the deep UV, near UV, and visible regions.[39,56] For example, a Ti:Sa laser system (Coherent Indigo-S) at Argonne National Laboratory generates continuously-tunable wavelengths in the 210–225 nm, 257–300 nm, 385–450 nm regions in addition to the 770–900 nm fundamental region, as shown in Fig. 3. This means that two wavelength regions are not available, 226–256 nm and 301–384 nm. More broadly and continuously wavelength-tunable Ti:Sa laser systems covering 700–960 nm are now commercially available. These lasers cover all the deep UV and wider visible regions.

3.2 Beam focusing and light collection for *in situ*/operando Raman measurements

Raman spectroscopy is a powerful *in situ* technique for studies of heterogeneous catalysis because it can provide vibrational spectra of the catalyst material itself, surface species including adsorbates, and gaseous reactants and products in a single measurement, under realistic reaction conditions (see Fig. 4). In this section, several methods of laser beam focusing and light collection for *in situ*/operando Raman studies (normal and resonance) are compared.

3.2.1 Room temperature measurements: small working distance and Raman microscope. Catalysts are typically activated by calcining up to ~700 °C under flowing reactive (oxidizing, reducing, *etc.*) or inert gases. If Raman data need to be recorded at room temperature before or after the pretreatments, the preferred working distance (see Fig. 4) of the collection optics is as small as possible to maximize collection efficiency, while

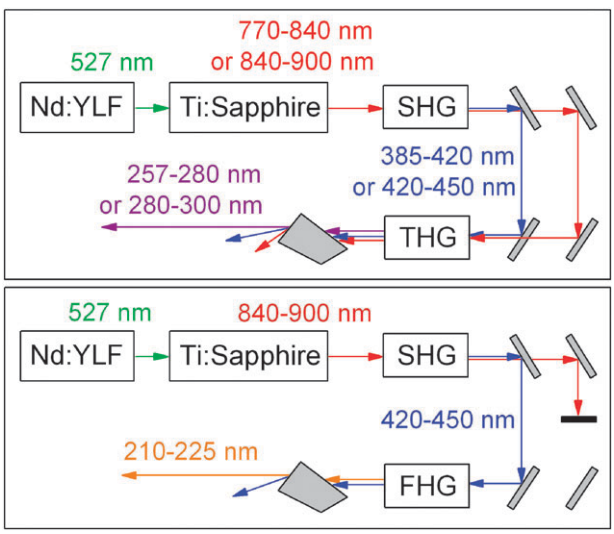

Fig. 3 Optical configurations for fundamental Ti:Sapphire, second- (SHG), third- (THG), and fourth-harmonic generation (FHG) output. A continuously-tunable, nanosecond-pulsed Ti:Sapphire laser is pumped by a Q-switched, intracavity frequency-doubled Nd:YLF laser.

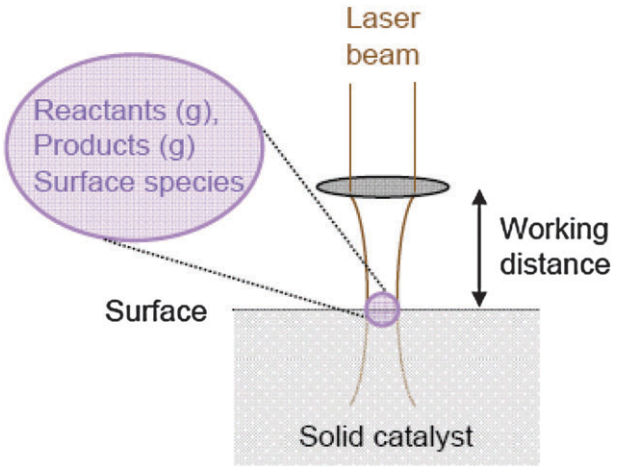

Fig. 4 Raman signals come from surface (and bulk solid) and gaseous species when the excitation laser beam focuses onto a solid catalyst. The working distance corresponds to the distance between the laser focus and the focusing or scattered light collection optical element.

matching the *f*-number of the spectrometer. At the same time the diameter of the focused laser beam decreases with the working distance (to be precise, *f*-number) of the focusing lens, which determines the resolution in spatially resolved Raman measurements. The beam diameter is given by: $w \propto \lambda f/d \approx \lambda l/d$, where w is the diameter (waist) of the focused laser beam, f is the focal length of the focusing lens, λ is the (excitation) laser wavelength, l is the working distance, d is the diameter of the delivery beam, f/d is the *f*-number ($f/\#$) of the focusing assembly.[59]

Raman microscopy has been widely used to study catalysts,[51,60,61] inorganic materials,[47,62] cells and tissues[63] or as a diagnostic tool for malaria.[64] In addition to spectroscopic information a small focused beam diameter, high collection efficiency, and imaging capability are the most important features of an objective-lens-based (Raman) microscope. The advantages basically come from the small working distances of objective lenses. The working distance of an objective lens in a typical UV Raman microscope[65] is 10.5 mm for a 36× magnification, 0.5 numerical aperture (NA) objective.

3.2.2 High temperature measurements: a large working distance and fluidizing conditions. As the working distance increases, the depth of field (DOF) also increases: DOF $\propto \lambda/\mathrm{NA}^2 \propto \lambda l^2$, where NA is the numerical aperture of the focusing lens or collection optics.[59] If the working distance of a collection optic and a focusing lens is larger, the corresponding volume sampled by the spectrometer is larger due to a longer depth of focus and a larger diameter focused beam. A long depth of focus can be important in Raman measurements under fluidizing (shaking and tumbling) conditions (see below)[5,6] where catalyst powder particles move in the vertical direction. The actual sampling volume may also be limited by the optical skin depth[6,66] and can be much smaller if the sample is a strong absorber at the excitation or scattered wavelength.

If Raman data need to be recorded under gas flow at high temperatures (*e.g.*, ~200 °C or higher), the working distance of both the beam focusing and collection optics should be as large as possible to avoid thermal effects. At large working distances it is easier to cool the optics that may be heated by their proximity to samples (and/or heating elements) at high temperatures. Moreover, temperature variations of the sample that may be caused by cooling the optics are easier to avoid.

3.2.3 *In situ* or operando Raman cell: fluidized bed *vs.* spinning or fixed bed designs. *In situ*[2,67] or operando[68] Raman measurements require a cell that can be used under the desired conditions. Various cell designs applied to heterogeneous catalysis have been described in reviews.[2,69] Relatively recently, *in situ* or operando Raman cells coupled to microscope objectives have been described in the literature.[60,70,71] More recently, commercially-available Raman cells have been applied to *in situ* or operando measurements.[52,72]

The laser beam focused onto the top surface of a solid sample (Fig. 4) may cause thermal- or photo-degradation. The sensitivity to degradation depends on the (1) thermal and optical properties of catalyst (thermal conductivity, specific heat, absorption coefficient at the laser excitation wavelength, *etc.*), (2) excitation laser power density at the sample, (3) residence time of the sample in the laser beam, and (4) the thermal- or photo-stability of the sample. These issues apply to any solid or liquid sample. For example, biological liquid samples have typically been circulated to decrease the residence time during UVRR measurements.[39,56]

Spinning solid catalysts in the form of a pressed pellet has been commonly used to decrease the residence time but is difficult to apply to *in situ*/operando measurements. The size and density of pressed pellets can lead to mass[73] and heat transfer[74] limitations and may be inappropriate for kinetics measurements. Another problem described in the early literature[75] is the measurement of sample temperature on high-speed spinning pellets. These problems are avoided with the fluidized bed (FB) cell.[5,6] The FB method is suitable for measurements of catalytic kinetics, flow-through reactions, and shortening the laser beam residence time. A comparison[5] between the FB, fixed bed, and spinning pellet methods shows that the FB method is the best for suppressing laser-induced degradation of adsorbates on solid catalysts and should be the method of choice for *in situ* and operando Raman experiments.

3.2.4 Light collection: lens *vs.* ellipsoidal reflector. The Asher,[37] Stair,[9] and Li[76] groups have used ellipsoidal reflectors to collect scattered light for UVRR studies. Fig. 5 shows a custom-designed 90° off-axis ellipsoidal reflector used by the Stair group at Argonne National Laboratory. This light collector has a much longer working distance than the reflectors described in previous publications by the Stair group.[5,9,77,78] Scattered light from the sample is collected by the reflector and focused onto the spectrometer entrance slit with a focusing cone matched to the NA of the spectrometer. The solid powder sample rests on top of a quartz frit in the FB *in situ*/operando Raman cell.[5,6] Although the collection efficiency of the new version ellipsoidal reflector is lower than the typical UV Raman microscope (NA ~0.18 *vs.* ~0.5), the working distance and depth of field are very large (~10 cm *vs.* ~1 cm and 20 μm *vs.* 2.5 μm at λ = 250 nm). These features are essential for Raman measurements using the high temperature, FB cell.

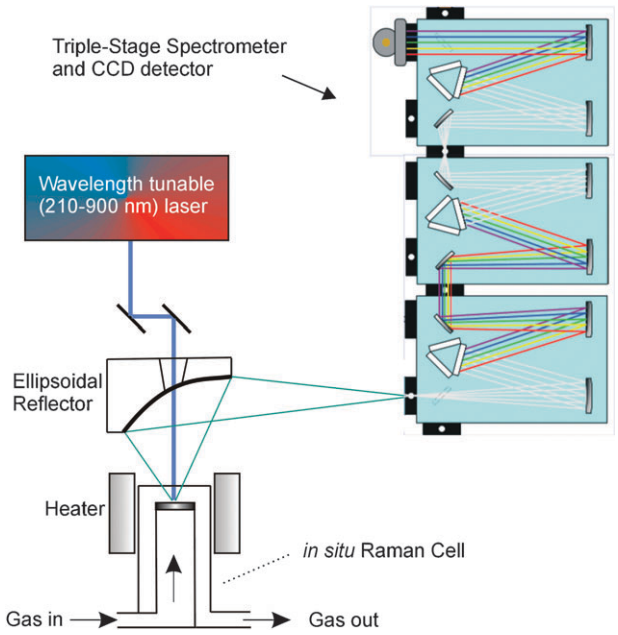

Fig. 5 UV resonance Raman system at Argonne National Laboratory. It consists of wavelength-tunable excitation lasers emitting from deep UV to near IR, a fluidized bed reactor (*in situ*, operando Raman cell), an ellipsoidal reflector for light collection, and a triple-grating spectrometer.

Single ellipsoidal reflectors have several advantages over other light collectors. These include (1) no chromatic or spherical aberration,[79] (2) higher throughput using only a single reflecting surface compared to a Cassegrain reflector or objective which requires two mirrors, (3) freedom from interfering signals produced by UV excitation of lens, beam splitter, or fiber optic materials used in lens-based or microscope collection geometries. Alternatively, the lens-based or microscope-objective-based collection systems exhibit very high efficiency and ease of use. These systems are available commercially and have been used extensively in many catalytic and noncatalytic applications where the features of the single ellipsoidal reflector are not critical.

3.3 Resonance Raman spectrometers: single-, double-, and triple-spectrometers

The advantages and limitations of three types of spectrometers (single-, double-, triple-grating) for resonance Raman studies are described in this section. The comparison is summarized in Table 1.

3.3.1 Single-spectrometer plus (notch or edge) filter. Stray light is mainly caused by undiffracted light at the face of the grating. It is generally more severe in shorter focal length or smaller *f*-number (*f*/#) spectrometers because the scattering from optical imperfections, dust, and reflections from interior components produces stray light that efficiently reaches the detector.[80] As the *f*/# of single-grating spectrometers decreases, the collection efficiency increases, but stray light and spectral resolution (dispersion) become limiting factors. UV operation requires higher dispersion spectrometers than visible Raman measurements because of the inverse proportionality between wavelength and wavenumber. For example, at 532 nm excitation, 0.1 nm corresponds to 3.5 cm^{-1} while at 210 nm, 0.1 nm corresponds to $\sim$23 cm^{-1}. Therefore, a long-focal-length spectrometer (1.26 m) and/or 2nd order diffraction (higher dispersion) have been used for UVRR studies.[42] Taken together, longer-focal-length single spectrometers show lower collection efficiency, but less stray light and higher dispersion (resolution) than shorter-focal-length single spectrometers.

Rayleigh (elastic) scattering is more intense than Raman scattering by $\sim 10^4$ times for liquids and gases and by $\sim 10^{10}$ times for solid powders and opaque crystals.[81,82] Single-grating spectrometers can attenuate Rayleigh scattering by $\sim 10^{-5}$ (at $\sim$100 cm^{-1} Raman shift)[81,82] and can be used without additional filters with transparent samples such as many liquids and gases. For solid powders and opaque crystals, an additional factor of at least $\sim 10^{-5}$ is required. Commercially available Rayleigh rejection (notch or edge) filters typically provide an additional factor of $\sim 10^{-5}$–10^{-6}. For experiments using multiple excitation wavelengths a separate rejection filter must be used for each wavelength. These filters are commercially available for commonly-used laser lines in the UV to near IR region. Filters coupled to single-grating spectrometers have frequently been employed in multiwavelength UV-vis RR (microscope) measurements on a wide variety of samples. They have the advantages of higher optical throughput and simplicity of operation compared to double- or triple-grating spectrometers.

3.3.2 Double- and triple-spectrometer. A single-grating spectrometer is not suitable for continuously wavelength-tunable RR measurements because a Rayleigh rejection filter would be required for each excitation wavelength. Double- and triple grating spectrometers can reduce Rayleigh scattering by $\sim 10^{-10}$ and $< 10^{-12}$ (or $\sim 10^{-16}$), respectively,[80,81] and are the instruments of choice with continuously tunable laser

Table 1 A comparison of spectrometers (single-, double-, and triple-grating) used for normal Raman or resonance Raman studies

	Single + filter[a]	Double	Triple
Rayleigh and stray light rejection	Good	Good	Excellent
Low Raman shift	Not good (deep UV), good (visible)	Good	Excellent
Discrete laser wavelengths	Compatible with proper filter[a]	Compatible	Compatible
Continuous laser wavelengths	Incompatible	Compatible	Compatible
Multichannel detection	Yes	Difficult, but possible	Yes
Optical throughput	Excellent	Good	Not good
Spectrometer complexity	Simple	Somewhat complicated	Complicated
Spectrometer price	Low	In-between	High

[a] Notch or edge filter for Rayleigh rejection.

systems. The high level of rejection allows triple-grating spectrometers to measure very low Raman shifts ($< \sim 50$ cm^{-1} in the visible, $< \sim 100$ cm^{-1} in the deep UV).

Triple-grating spectrometers require more optical reflections (typically, 10–12 mirrors and 3 gratings), as shown in Fig. 5. The associated losses result in significantly lower optical throughput than single- or double-spectrometers. The first two stages efficiently filter out Rayleigh and stray light. The third-stage operates as a spectrograph to disperse the spectrum onto either a UV-enhanced CCD (charge-coupled device) or an IPMT (imaging photomultiplier tube)[9] detector.

Double-grating spectrometers are incompatible, in general, with multichannel CCD or IPMT detectors, while triple-spectrometers have been specifically designed to work with them. Since the width of the middle slit in a double monochromator must be small to reduce stray light to an acceptable level, the corresponding spectral bandpass does not cover the entire detector area. Effective use of multichannel detection in a double spectrometer requires a wide middle slit, which leads to increased stray light.[83] In some RR applications, such as biological studies where maximal optical throughput is desired, a wavelength-tunable (deep UV) laser is used, and the low-Raman-shift region is not important, a double monochromator can be the best choice.[39]

4. UV Raman and the problem of Raman backgrounds

4.1 Three sources of Raman background

The "Raman background" or so-called "fluorescence background" has been a major hindrance to the application of Raman spectroscopy in studying not only solid catalysts[2,6,84] but also a wide variety of other materials such as biomolecules,[85,86] plant cells,[87] polymers,[88] paintings and textiles,[89] biomedical,[90–92] pharmaceutical,[92,93] and forensic materials.[94]

The background has been widely attributed to fluorescence since the early Raman studies of oxide surfaces[95,96] and biopolymers and proteins.[97] However, a strong anharmonic interaction has also been suggested as an alternative to fluorescence. Since fluorescence can originate from defect states in solids as well as fluorophores, more than one source may simultaneously contribute to the Raman background (*e.g.*, fluorophore plus defect fluorescence or defect fluorescence plus anharmonic interaction), and one source may affect the other. For example, the presence of cation (Al^{3+}) vacancies at the γ-Al_2O_3 surface can significantly modify surface electronic structures responsible for defect fluorescence and can also affect[98] the distribution of surface OH frequencies related to anharmonic interactions. Three distinct sources are described in the following sections.

4.2 Raman (fluorescence) background due to fluorophores

The Raman background can be attributed to fluorescent molecules or ions (fluorophores), which are impurities or part of the sample itself. If the fluorophore is a trace transition metal impurity (*e.g.*, surface or bulk Fe^{3+}, Cr^{3+}), specific impurity energy levels are present (see below). If the fluorophores are organic impurities (*e.g.*, dyes, oils, lubricants, greases), they may be removed or quenched by heating in oxygen or purification. If the removal or quenching process is difficult or undesirable (*e.g.*, the fluorophore is the sample itself or the process changes the surface structure or catalytic properties), the fluorescence background may be unavoidable.

4.3 Defect fluorescence

4.3.1 Evidence for Raman background from defects. All solids contain intrinsic point defects[99] and high surface area materials naturally contain many defects.[100] Most high surface area metal oxides exhibit a strong Raman background.[101] γ-Al_2O_3 and η-Al_2O_3 contain many crystallographic defects,[102] while θ-Al_2O_3 and α-Al_2O_3 are relatively defect-free (intrinsically lower surface area).[103] From our observations the former show much stronger Raman backgrounds than the latter. This suggests a possible connection between defects and Raman backgrounds.

An early experimental study by Nelson and Hale[104] showed that the presence of point defects (produced by γ- or neutron-irradiation and identified by ESR) in high surface area MgO generates several absorption bands with transition energies that are much lower than the bulk MgO bandgap of 8.7 eV (142.5 nm). In particular, two broad absorption bands at $\lambda_{max} \approx 600$ nm (F_s^+ center, single electron in a surface anion vacancy) and at $\lambda_{max} \approx 1240$ nm (S_H center, F_s^+ center with nearby –OH groups) disappear and reappear in the presence and absence of O_2 at room temperature, respectively. Similarly, Tench and Pott[105] observed that the addition of O_2 gas to MgO at room temperature destroys the $\sim$420 nm photoemission induced by $\lambda_{max} \approx 250$ nm excitation that is associated with another oxygen vacancy site (F^+ center).[104] These observations confirm that the O_2 adsorption sites are associated with oxygen vacancy sites and with photoabsorption and photoemission sites. The fact that the excitation wavelengths used in conventional Raman spectroscopy are within the contour of the intense absorption band maximum at $\sim$600 nm (FWHM $\approx$ 200 nm) suggests a possible connection between the oxygen vacancy sites and the Raman background.

Although hydrocarbon impurities are a known source of Raman background and can be removed by heating in oxygen,[96,101] the photoabsorption and photoemission described above are unrelated to hydrocarbons because both Nelson's and Tench's MgO materials were hydrocarbon-free. The addition of O_2 gas to impurity-free η-alumina was found to suppress the Raman background.[101] This observation supports the connection between the Raman background and oxygen adsorption sites. Taken together, all of the prior work provide support for a connection between vacancy or defect sites and the Raman background.

4.3.2 Connection between Raman background and excitons. To our knowledge, the first experimental result showing a direct connection between defect fluorescence assigned to excitons (defect-related fluorescence) and the Raman background was by Helfrich and Lipsett for impurity-free, melt-grown and vapor-phase anthracene crystals.[106] Jeziorowski and Knözinger[101] also suggested that the Raman background

could originate from emission by excitons bound to surface centers associated with the crystalline defects of η-Al_2O_3. Excitons are Coulomb-correlated electron–hole pairs and can be excited by photons or electrons. The deactivation or (re)-combination of excitons typically produces light emission (fluorescence or phosphorescence).[107,108] In a relatively recent report by Splett *et al.*[109] the Raman background from a hydroquinoline crystal excited at 633 nm significantly increased after melting and rapid cooling to produce crystal defects. Therefore, the presence of crystalline defects (including dispersed metals with an island structure, protonated oxygen bridges in perfect zeolites, and even crystals near the melting point) has been suggested to be important for the Raman background.[109]

4.3.3 Defect energy levels. Solid surface electronic states may differ in energy from the bulk band structure due to the change in symmetry. Surface ions can be considered[110] "equivalent" to ions in the bulk of ionic crystals, but will experience reduced Madelung energy. Thus, the ratio ($\varepsilon = E_{sg}/E_{bg}$) of surface ($E_{sg}$) to bulk bandgap ($E_{bg}$) is expected to be less than one ($0 < \varepsilon < 1$).[110] A recent theoretical (*ab initio*) comparison of the electronic structures for the bulk and (001) surface of γ-Al_2O_3 obtained a value for E_{sg} that is smaller than E_{bg} by 0.9 eV, probably due to different electrostatic interactions at the surface compared to the bulk.[111]

The presence of the steps and corners at the surface can produce new surface energy states, located in the bulk bandgap, that can trap electrons, *e.g.*, cation terminated step-corner.[112] Surface states (O_{3C}^- site where '3C' means 3-coordinate), localized at the oxygen-terminated corner of MgO surfaces, are a source of fluorescence (singlet to singlet transition) at 3.3 eV induced by the photoabsorption at 4.6 eV which is much lower in energy than the bulk bandgap.[108,113]

The presence of other types of defects such as cation-, anion-, and neutral-vacancies along with (ion) impurities either in the bulk or at the surface generates their specific electronic states in the bandgap referred to as "defect energy levels" and "impurity energy levels", respectively. The visible colors of Ruby (red) and Sapphire (blue, yellow, *etc.*) due to trace amounts of Cr, Fe, Ti, *etc.* impurity ions in α-Al_2O_3 (bandgap in the vacuum UV region) are the direct result of impurity energy levels. One theoretical[114] study shows that defect light emission originates only from surface defects (adatoms, steps, and vacancies) in inorganic solids (semiconductors, alumina) and is not observed from the defect-free surfaces. The defect energy levels (oxygen or Al vacancy, *etc.*) in aluminas (α-, θ-, η-, and κ-Al_2O_3),[115–121] MgO,[122] and semiconductors (ZnO, CdS, Boron carbide)[123–125] have been obtained theoretically or experimentally. For example, electron energy loss spectroscopy[126] found a bandgap of 2.5 eV ($\lambda = 496$ nm) that is associated with a defect energy level at the γ-Al_2O_3 surface. This energy is close to the photon energy used in conventional Raman spectroscopy and is much smaller than the bulk bandgap.

4.4 Avoidance of defect fluorescence by UV Raman spectroscopy: γ-Al_2O_3 as an example

The acquisition of Raman spectra from γ-Al_2O_3, one of the most widely used catalyst supports, has long been unsuccessful. γ-Al_2O_3 has been designated as "Raman silent or Raman inactive or featureless in Raman",[127–132] in measurements using laser excitation in the visible or near IR region. One successful Raman measurement, to our knowledge the only report in the literature, was given by Spielbauer.[133] Very weak Raman bands attributed to γ-Al_2O_3 were detected at 846 cm^{-1} and 256 cm^{-1} with 488 nm excitation on top of a strong Raman background.

The fluorescence background can be significantly reduced or avoided with UV excitation because the defect emission (fluorescence and phosphorescence) appears predominantly in the near UV to near IR region. With 244 nm excitation, a clear Raman band has been observed[134] centered at ~855 cm^{-1} for γ-Al_2O_3. This demonstrates that deep UV excitation is important to obtain spectra from weak Raman scattering materials, such as γ-Al_2O_3, when they are in a highly defective, high surface area form.

4.5 Avoidance or suppression of fluorescence, in general

Fluorescence is typically ~10^{11} times and ~10^3 times stronger than nonresonance Raman and resonance Raman scattering, respectively.[135] Consequently, fluorescence from even a minor fluorophore concentration can render the background too intense to detect the Raman spectrum.

One powerful technique to avoid fluorescence interference makes use of time-gating methods, either pulse-gating[136,137] or optical Kerr-gating.[88,90] These methods use a picosecond pulsed excitation laser and a synchronized, gated detector (and Kerr-medium for Kerr-gating). Time-gating methods take advantage of the difference between the ultrashort Raman lifetime, of order[138,139] 10^{-11}–10^{-13} s, and the relatively long fluorescence lifetime, of order 10^{-6}–10^{-9} s for most solutions and solids.[139,140] Another recently developed technique is femtosecond stimulated Raman spectroscopy (FSRS)[141,142] which combines a picosecond Raman pump pulse and femtosecond Stokes probe pulse. The ultrashort time-resolution, which minimizes the fraction of detected background fluorescence, and the directional nature of the detecting laser pulses combine to make FSRS exceptionally powerful in rejecting fluorescence background. The drawbacks of these methods are (1) the potential for sample degradation induced by the high peak power associated with very short laser pulses, (2) the limitation to excitation wavelengths in the visible to near IR region, (3) in FSRS, the weaker Raman scattering in 180° backscattering geometry than 90° configuration.[143] The 180° geometry is more convenient for many catalytic studies.

Fluorescence backgrounds appear primarily in the visible and sometimes near IR (NIR) region[144] and are associated with the CW visible (sometimes NIR) excitation lasers used in conventional Raman spectroscopy. It can largely be avoided using ultraviolet laser excitation. In UV Raman (Stokes or anti-Stokes) the features of interest due to vibrational transitions are in the ultraviolet region at wavelengths near the excitation laser and at much higher energy than fluorescence. The application of UV Raman spectroscopy to avoid fluorescence in measurements relevant to heterogeneous catalysis has been discussed in previous reviews.[6,84]

4.6 Raman background due to strong anharmonic interaction

A source for the Raman background distinct from fluorescence was first suggested in the early-70's. For example, Careri *et al.*[145] reported a correlation between the Raman background intensity excited at 488 nm and the amount of water that is tightly hydrogen-bonded on the surface of proteins and oxides such as γ-Al_2O_3. They concluded that the background cannot be explained by ordinary fluorescence. Biscar and Kollias similarly concluded that the Raman background they observed is not associated with fluorescence, but Raman-like[146] on the basis of the position of the background obtained from albumin proteins using several different excitation wavelengths of an Ar^+ laser. Later, Jeziorowski and Knözinger[147] also observed a similar correlation between the intensity of the Raman background (although they described it as "fluorescence") excited at 514.5 nm and the density of surface hydroxyl groups on MgO and η-Al_2O_3. They concluded that the background is an intrinsic property of hydroxylated oxide surfaces and cannot be removed by sample treatments unless all hydroxyl groups are eliminated.

In the 90's, a close correlation between the intensity of the background and the acid strength of zeolite OH groups was observed.[148] Mortensen *et al.*[144] and Chen *et al.*[149] also concluded that the Raman background from alumina excited in the visible and near IR region is not caused by fluorescence. Interestingly, Splett *et al.*[109] discerned two distinct contributions to the Raman background, namely "defect fluorescence" (as described above) and "hydroxyl groups" (between the hydroquinoline crystal and water). The difficulties in removing both the Raman background and the surface OH groups from oxide materials are consistent with each other. For example, the surface OH densities on alumina after heating to $\sim$650 K and $\sim$800 K are still 50% and 33%, respectively, of the density on fully hydrated alumina.[150]

The non-fluorescent contribution to Raman backgrounds has been discussed in detail by Ostrovskii *et al.*[151] as a strong anharmonic interaction between high-wavenumber vibrational excitations (X–H, where X = O, C, *etc.*) and low wavenumber phonons (lattice vibrations). Their interpretation is supported by experimental and theoretical results from organic and inorganic materials such as crystal hydrates, tooth enamel (a non-hydrated material containing OH vibrations), and polymers that include O–H or C–H bonds. For example, poly[vinylidene fluoride] with the formula $-[CF_2CH_2]_n-$ is characterized by high-wavenumber ν(C–H) vibrations and shows a strong Raman background. In contrast, poly-[tetrafluoroethylene] with the formula $-[CF_2CF_2]_n-$ has no vibrations above 1500 cm^{-1} and is free of the background (see Fig. 7 of ref. 151).

Anharmonic coupling has been directly observed in simple molecules. For example, Kukura *et al.*[141] observed anharmonic coupling in deuterated chloroform between the high frequency C–D stretch and the low frequency, totally symmetric bend vibrations in the time domain with FSRS. In the Raman spectra of hydrogen-bonded liquids such as alcohols, the combination of Fermi resonance and anharmonic coupling between the hydrogen-bonded OH vibrations and low frequency vibrational modes is responsible for a very broad band in the OH stretching region.[152] In hydrogen-bonded solids, strong anharmonic coupling between high-frequency ν(X–H) and low frequency lattice-vibrations can be predicted theoretically. The coupling is responsible for a very broad band that is red-shifted from the position of high-frequency band and whose shape depends on the anharmonic coupling constants and a damping constant.[153,154]

5. Second problem of normal Raman (detection sensitivity) and solution by UVRR

5.1 Detection limit of Raman and UVRR for bulk species

The sensitivity or detection limit in Raman spectroscopy depends on the intensity of the bands (magnitude of the Raman cross sections) for the chemical species of interest compared with those of overlapping or interfering Raman bands and other sources of emission from the sample or impurities. Total (full solid angle of 4π steradians) scattering cross sections are typically of order 10^{-29} cm^2 per molecule for normal, nonresonance Raman scattering and of order 10^{-18} and 10^{-21} cm^2 per molecule for absorption (or fluorescence) in UV and IR, respectively.[155] Therefore, sample concentrations greater than 0.01 M are generally required for detection by normal Raman spectroscopy assuming $\sim 10^4$ Raman photons per second with laser excitation at 100 mW of 514.5 nm. Because the cross section for resonance Raman scattering can be of order 10^{-22} cm^2 per molecule (*i.e.*, 10^7-fold resonance enhancement), the detection limit for resonance Raman spectroscopy can be nM (nanomoles per liter) or of order ppb (parts per billion), and even as low as ppt (parts per trillion) concentrations.[135] For example, detection limits of 14 μM (200 ppb) for both NO_2^- and NO_3^- and 10^{-7} M (20 ppb) for both pyrene and anthracene in solution have been obtained by UV resonance Raman spectroscopy.[156,157]

5.2 Detection limit of Raman and UVRR for surface species

The signal from a surface monolayer in normal Raman spectroscopy is expected to be roughly 10^5 weaker than a typical bulk sample.[80] The factor of 10^5 was obtained from the ratio of the pathlength ($\sim$100 μm) for transparent bulk samples to the thickness of a surface monolayer ($\sim 10^{-3}$ μm or $\sim$1 nm). Despite the intrinsic difficulty, adsorbed molecules (*e.g.*, nitrobenzene) on a Ni(111) single crystal at sub-monolayer coverages have been detected[158] by normal (non-resonance, non-surface-enhanced) Raman spectroscopy. However, this type of measurement is by no means routine. It is only feasible for strong Raman scattering adsorbates on surfaces that produce exceptionally low background emission. When the substrate material has a large Raman scattering cross section (*e.g.*, TiO_2 with visible excitation), then Raman bands from the substrate can screen the bands from surface species. When the substrate or impurities produce background emission, the background can easily overwhelm the surface Raman signal. These issues highlight the potential difficulties of surface Raman spectroscopy without resonance enhancement and background suppression.

The fluorescence background can be significantly suppressed by deep UV excitation as discussed above. If the UV-wavelength

excitation is resonant with an electronic absorption of the surface species, even trace amounts can be detected. For example, a strongly-enhanced MoO stretching vibration excited at 244 nm has been observed by Li and coworkers from a 0.1 wt% MoO_3/γ-Al_2O_3 (S_{BET} = 242 m^2 g^{-1}).[10] 0.1 wt% corresponds to a surface density of ~0.03 Mo atoms per nm^2 or ~0.003 ML, assuming one monolayer (ML) corresponds[159] to 10 atoms per nm^2. Since the MoO band was observed with a signal-to-noise of ~40, we estimate the detection limit is at least ~0.001 ML. A similar detection limit has been observed[134,160] for V/θ-Al_2O_3 by UVRR excited at 244 nm. The typical detection limits for UVRR and other spectroscopic techniques are summarized in Table 2.

5.3 Sum frequency generation vibrational spectroscopy (SFG-VS)

SFG-VS is based on a second order nonlinear optical process, which is forbidden in centrosymmetric media (*i.e.* bulk gases, liquids, and solids with inversion symmetry under the electric-dipole approximation) but allowed at a surface or interface between two centrosymmetric media where the inversion symmetry is broken.[166] It is a surface specific technique and can be applied to molecules adsorbed on single crystals, thin films, metal foils, and supported nanoparticles.[167] Regarding SFG-VS selection rules, the resonant nonlinear susceptibility that is directly connected to the intensity of SFG signals includes the product of vibrational IR and Raman transition moments.[167] Accordingly, a vibrational mode must simultaneously satisfy both IR and Raman selection rules in order to be SFG active. For example, SFG is not allowed for media such as alkane chains on planar surfaces in an ordered all-*trans* conformation because of inversion symmetry around the CH_2 groups.[168] Therefore, SFG-VS provides information that is complementary to IR or Raman data. This can result in significantly simplified spectra for systems with spectral congestion.

The detection limit of SFG is commonly regarded as at the monolayer or submonolayer level.[166] With optical heterodyne detection (HD-SFG)[169] the detection limit is substantially decreased in the CH stretching region to a few percent of ML coverage. An extraordinary SFG detection limit of ~0.001 ML (or lower) for CO adsorbed on Ru(001) at 390 K has been reported.[162] Although the detection limits of SFG and UVRR are roughly the same (see Table 2), SFG has high sensitivity for high frequency (CO, NO, CH, and OH, NH stretching) vibrations, while UVRR covers the low frequency region where M–O, M=O, M–O–S, and M–O–M vibrations (M: metal, S: support) appear.

5.4 Polarization modulation infrared reflection-absorption spectroscopy (PM-IRAS)

IRAS (infrared reflection-absorption spectroscopy)[167] (also RAIRS: reflection-absorption infrared spectroscopy), like Raman, provides vibrational spectra of gases and liquids as well as adsorbed species on reflecting surfaces. Using gas or liquid phase detection, the concentrations of reactants and products can be measured as a complement (or replacement) to conventional analytical tools such as gas (liquid) chromatography or mass spectrometry. PM-IRAS denotes IRAS combined with s- and p-polarization modulation of the IR beam. With p-polarization (perpendicular to a reflective surface) both surface and gas (liquid) phase species are detected. With s-polarization (parallel to the reflective surface) only the gas (liquid) phase species are detected. The difference in IR signals generated from p-polarization and s-polarization produces surface-specific IR spectra. The dual selectivity combined with a nearly simultaneous measurement of bulk and surface species can be an advantage of PM-IRAS over other techniques such as SFG, ATR-IR (attenuated total reflectance IR), and Raman spectroscopy.[170]

An extraordinary IRAS detection limit of ~0.001 ML for CO adsorbed on Ru(001) at 30 K has been reported. The detection limit at room temperature or high temperature is degraded by thermal noise. A more typical IRAS detection limit is ~0.01 ML for CO adsorbed on Pd or Pt.[163] A detection limit of ~3 μM for benzopyrene on Au in solution has been observed by probing aromatic CH stretching bands in PM-IRAS spectra.[164] PM-IRAS, similar to SFG-VS, is particularly useful in the high frequency region. Compared to Raman spectroscopy the performance of PM-IRAS does not match Raman spectroscopy for low frequency vibrations and at high temperatures.

5.5 Extended X-ray absorption fine structure (EXAFS)

The typical detection limit of EXAFS is considered to be of order tens of ppm.[161] Although a detection limit of ~10^{14} Au atoms per cm^2 (= 1 Au atom per nm^2 ~0.1 ML) in silicon has been achieved[165] by grazing incidence Au-Lα fluorescence detection, the limits for UVRR and SFG are two orders of magnitude better (see Table 2). This is consistent with a recent observation[160] that UVRR is sufficiently sensitive to distinguish between monomeric and dimeric vanadium oxide supported

Table 2 Sensitivity (detection limit) comparison of UV Resonance Raman (UVRR) with other common spectroscopic techniques. PAH is an abbreviation of polycyclic aromatic hydrocarbons

	Sensitivity (detection limit)	
	Bulk	Surface density or monolayer (ML)
SFG		~0.001 ML CO on Ru(001) at 390 K[c]
PM-IRAS		~0.01 ML CO on Pt or Pd,[d] 3 μM PAH in solution on Au[e]
EXAFS	Tens of ppm[a]	~0.1 ML (1 Au atom per nm^2 for Au in Si)[f]
UVRR	0.1 μM (20 ppb) PAH in solution[b]	~0.001 ML (0.01 M atoms per nm^2 where M = V, Mo in MO_x)[g]

[a] Ref. 161. [b] Ref. 156. [c] Ref. 162. [d] Ref. 163. [e] Ref. 164. [f] Ref. 165. [g] Ref. 84, 134 and 160.

on alumina (both are ~0.1 V atoms per nm^2 ~0.01 ML), while EXAFS was not.

6. Additional advantages of UVRR

While the main application for resonance Raman spectroscopy is the identification and monitoring of molecular and surface species in catalysis, in this section we summarize how the spectroscopic details can provide additional information on their atomic and electronic structures.

6.1 Selective resonance enhancement of Raman bands

Vibrational Raman bands attributed to a specific molecular species or chromophore in a complex mixture can be selectively enhanced by RR spectroscopy. Ref. 171 provides a number of examples in a variety of fields including (1) selective detection of lycopene, β-carotene, and polycyclic aromatic hydrocarbons such as pyrene, (2) selective identification of natural dyes that were used to color old printed papers, (3) selective characterization of single-walled carbon nanotubes mixed with other carbon nanotubes, (4) selective study of single-stranded DNA genomes or metalloproteins mixed with other proteins. A very recent review describes developments on chromophore-specific RR spectroscopy theory that can be used to study photochemical and photophysical processes in large molecules.[17]

Specific vibrational modes within a molecular complex can be selectively enhanced unless the modes are strongly coupled to other modes. Four examples follow. First, UV excitation of the heme–cyanide complex causes strong, selective enhancement of the vinyl C=C stretching Raman intensity, while little enhancement occurs for the heme vibrational modes.[172] This selective enhancement is evidence for non-conjugation of the vinyl group with neighboring organic functional groups in heme.[172] Second, the (totally-symmetric) porphyrin C–N stretching Raman band of deoxy-hemoglobin[173] is selectively enhanced when the laser excitation energy approaches the Soret electronic absorption band.[174] Third, the totally symmetric O–H stretching Raman band of H_2O is selectively enhanced together with the appearance of overtones (up to 5th order) with excitation at ~160 nm, which is resonant with the X → A electronic transition of H_2O. The bending vibration is selectively enhanced with the excitation at ~141 nm, which is resonant with the X → B transition.[175] Fourth, two modes of the same type of vibration, but with different symmetries, can be distinguished by selective resonance enhancement. For example, only the totally symmetric A_1 mode is selectively enhanced in the two S–Fe–S bending modes appearing at 130 cm^{-1} (A_1) and 150 cm^{-1} (E) in the RR spectra of rubredoxin (a simple iron–sulfur protein) when excited at ~497 nm which corresponds to a dipole-allowed electronic transition.[173]

For the monomeric O=V–$(OAl)_3$ surface species in alumina supported vanadium oxide, V=O and V–O stretching modes are selectively enhanced in RR spectra[1] excited at 220 nm and 287 nm, respectively (see Fig. 6). V=O overtones are quite intense with 220 nm excitation where the V=O fundamental band is most strongly enhanced. In contrast, V–O overtones are very weak with 287 nm excitation where the V–O fundamental is most strongly enhanced. The difference in overtone intensity is indicative of a significant increase in the V=O bond length and a negligible increase of V–O bond length in the corresponding excited electronic states. Quite recently, a similar RR result has been reported[52] showing the selective enhancement of the V=O stretching mode for silica supported vanadium oxide with 244 nm excitation. These RR results can provide insight into the details of photo-induced catalytic reactions that involve these excited states (see below).

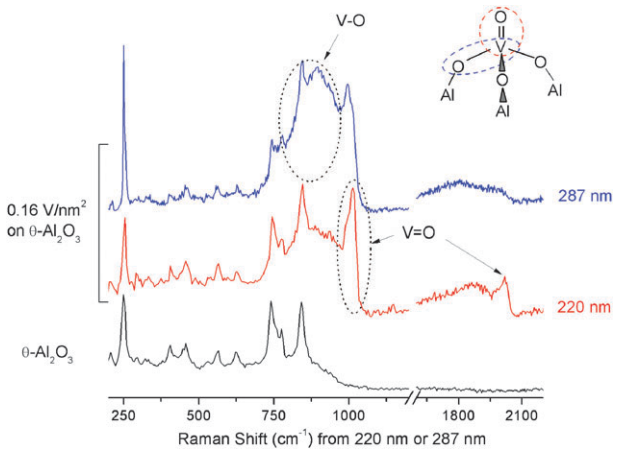

Fig. 6 UV resonance Raman spectra excited at 220 nm and 287 nm for alumina supported vanadium oxide monomers. The symmetric V=O stretching mode is selectively enhanced with 220 nm excitation, while the symmetric and asymmetric V–O stretching modes are selectively enhanced with 287 nm excitation. A detailed vibrational assignment is available in ref. 1.

6.2 Elongated V=O induced by UV: photocatalytic active site

Extensive studies by phosphorescence spectroscopy (PS)[176–184] reveal that: (1) monomeric (isolated) VO_4 tetrahedra supported on silica or alumina are good photoactive catalysts for CO oxidation and selective oxidation of alkanes, olefins, and alcohols in the presence of oxygen. (2) The phosphorescence center is the triplet excited state of the elongated, axial V=O bond. (3) The bond length increase, 0.12 Å, and V=O frequency, ~1050 cm^{-1}, can be obtained by Franck–Condon analysis of phosphorescence spectra[182] for silica supported vanadium oxide at 77 K.

The photocatalytic activity (quantum yield for photo-oxidation) of supported vanadia correlates with the phosphorescence intensity suggesting a role for the phosphorescence center in the reaction. A detailed photoactivation mechanism was recently described by Teramura *et al.*[183] In this mechanism, interestingly, activation of either the axial V=O by 250 nm excitation or the basal V–O by 330 nm excitation leads to the same triplet excited state localized on the V=O bond *via* intersystem crossing. The 250 nm and 330 nm excitations in the PS experiments match well with the 220 nm and 287 nm excitations in our RR experiments, in terms of the selective excitation of V=O and V–O vibrations. RR results (Fig. 6) are consistent not only with elongation of the V=O bond *via* 220 nm excitation and an enhancement of the V–O with little elongation at 287 nm excitation, but also strong elongations of V=O with 287 nm excitation and of V–O vibrations with

220 nm excitation, where all of the excited states are singlets.[1] The RR results are complementary to PS by providing information about the excited singlet state.

The RR results provide values for the increase in V=O and V–O bond lengths of 0.09 Å with 220 nm excitation and 0.01–0.02 Å with 287 nm excitation, respectively.[1] While these results were obtained at 295 K, the spectroscopy measurement can be performed at any temperature. The value obtained for the V=O bond length change in the excited singlet state is comparable to the value of 0.12 Å obtained by PS.

6.3 RR and the assignment of UV-vis absorption bands

UV-vis absorption/reflectance spectroscopy[185] provides useful information on the coordination and oxidation states of metals, the energies of electronic excitations, and so on. The measurements can be performed under high temperature and pressure reaction conditions and have been frequently employed to investigate solid catalysts. The spectra can be calculated for systems with well defined structure that are not too large.[186] However, the assignment or interpretation of UV-vis absorption bands is often unclear or controversial. The broad (typical FWHM $\approx$ 2400–15 000 cm^{-1}),[187] overlapping nature of typical UV-vis bands is largely responsible for this ambiguity. In addition, the structure of high surface area supports and of oxide monolayers on the supports, the catalytic materials of interest, are poorly-defined and inhomogeneous making it difficult to directly compare experimental data with a reference material or calculation. Resonance Raman spectroscopy is a powerful technique for assigning the electronic transitions observed in UV-vis absorption spectra because of the direct link between the vibrations that are enhanced and the electronic transition responsible for the absorption.[12,188] This section describes the assignment of UV-vis absorption bands by RR. To facilitate the discussion of the RR-based method, we begin with a brief review of three commonly-used assignment methods.

6.3.1 First method to assign vanadia UV-vis absorption bands. The first method for assigning UV-vis absorption bands utilizes an empirical correlation[189] between the position of longest-wavelength charge-transfer band (E_L in eV or λ_L in nm) in the UV-vis spectra and the vanadium coordination number in reference compounds, *i.e.*, Na_3VO_4, $NaVO_3$, α-VPO_5, and V_2O_5. The reference compounds and supported vanadium oxides show at least two charge-transfer (CT) bands in the 200–500 nm region (see Table 3). The position of the λ_L band gradually shifts to longer wavelength (or to a new λ_L band) as the vanadium loading or coordination number increases from tetrahedral (T_d) to square pyramidal to octahedral (O_h) coordination. For example, all T_d reference vanadium oxides and supported vanadium oxides with low V loadings have CT bands only in the UV region. V_2O_5 (O_h) and supported vanadium oxides with high V loadings show a characteristic CT band in the visible region, *e.g.*, ~455 nm. The average position of the 2–3 CT bands also gradually shift to longer wavelength as the vanadium loading or coordination number increases because the short-wavelength CT λ_S bands do not shift as much as the λ_L band.

6.3.2 Second method to interpret UV-vis spectra. The second method uses a linear correlation between the absorption edge energy in the 354–564 nm region measured for a number of reference compounds and their degree of polymerization (number of V–O–V bonds)[195] or degree of condensation (number of V atoms in the 2nd coordination sphere).[196] Many authors who interpret their UV-vis spectra following first or second method do not make mention of the other method. This gives the impression that the two methods are distinct. However, the two methods are essentially equivalent because the peak and the edge of the low energy CT band track each other with a separation corresponding to the half-width at the baseline of the CT band. For example, the CT band positions for NH_4VO_3 (T_d) and V_2O_5 (O_h) differ by 0.8 eV,[187] and their edge energies differ by the same amount.[187]

6.3.3 Third method to assign UV-vis absorption bands. The short-wavelength CT (λ_S) bands have always been observed[191,192,196–198] in supported vanadium oxides and their reference compounds with both T_d and O_h symmetry. Busca *et al.*[199] and Centi *et al.*[192] provide assignments for some, but not all, of the λ_S bands. Since the work of Centi *et al.*[192] is one of the most cited in publications where UV-vis spectroscopy has been applied to characterize vanadium oxides,[187] it is

Table 3 Positions of charge transfer bands, λ_{CT} observed in UV-vis spectra for reference vanadium compounds, VO bond lengths obtained by the linear equation of 1.224 + 0.00174λ_{CT} (R_{VO}), and by X-ray crystallography ($R_{VO,X\text{-}ray}$)

	λ_{CT} in nm from UV-vis[a]	R_{VO} in Å	$R_{VO,X\text{-}ray}$[c] in Å
Na_3VO_4: monomeric VO_4, distorted T_d	238	1.64	1.68
	290	1.73	1.70 (3×)
α-$NaVO_3$: 1-dim chain VO_4,	—[b], 233	—, 1.63	1.63
T_d with two bridging oxygen	275, 286	1.70, 1.72	1.65
	340, 345	1.82, 1.82	1.80–1.81 (2×)
NH_4VO_3: 1-dim chain VO_4, T_d with	220, 233	1.61, 1.63	1.65
two bridging oxygen	290, 286	1.73, 1.72	1.67
	370, 357	1.87, 1.85	1.80 (2×)
V_2O_5: distorted O_h with a very long	238, 250	1.64, 1.66	1.58
V–O bond, VO_5 square pyramid	323, —[b]	1.79, —	1.78
	363, 357	1.86, 1.85	1.88 (2×)
	454.5, 465	2.01, 2.03	2.02
	—[b]	—	2.79

[a] Ref. 189, 190 for Na_3VO_4, ref. 189, 190, 187 for α-$NaVO_3$, ref. 191, 187 for NH_4VO_3, and ref. 192, 187 for V_2O_5. [b] Unavailable in the references, but can be estimated from the equation and bond length, *e.g.*, 900 nm for 2.79 Å of V_2O_5. [c] Ref. 193 and 194.

important to examine the assignments carefully. Centi's assignments[192] can be summarized as follows: (1) CT bands in the region 286–333 nm (35 000–30 000 cm^{-1}) are related to T_d V^{5+} species, based on the work of Ronde and Snijders[200] (see below), (2) CT bands in the range 333–500 nm (30 000–20 000 cm^{-1}) are due to O_h V^{5+} species, (3) the CT bands near 385 nm (26 000 cm^{-1}) for V_2O_5 (and other 5- or 6-coordinated compounds) are due to the V=O bond. Centi's assignments (1) and (2) are virtually the same as method one. Assignment (3) has frequently been cited by other researchers, but we believe it is incorrect. An important piece of evidence for assigning the 385 nm band to V=O bond is the match with the value obtained in the expression by So and Pope.[201] However, this expression corresponds only to the lowest CT energy, not the CT energy of V=O.

6.3.4 A new fourth method to assign UV-vis absorption bands. A new method for assigning UV-vis CT bands is based on RR results.[1] This method is in agreement with methods 1–3 and can be considered as a band-specific unified method.

Ronde and Snijders[200] found a smooth correlation between the average VO bond length, $R_{VO,AVG}$ in the 1.65–1.82 Å range and the average position of the first two CT bands, $\lambda_{CT,AVG}$ in the 243–335 nm region obtained by experiment and calculation for T_d and spinel (mixture of T_d and O_h) vanadium oxides. A linear-fit with $\lambda_{CT,AVG}$ in nm and $R_{VO,AVG}$ in Å has been extracted[1] by digitizing Ronde's scatter data.[200]

$$R_{VO,AVG} = 1.224 + 0.00174\lambda_{CT,AVG}$$

This correlation was obtained primarily from T_d compounds, with some contribution from O_h compounds due to the spinel reference compounds. The average VO bond lengths for the 4-, 5-, and 6-coordinated reference vanadium oxides are 1.69–1.74 Å, 1.79–1.95 Å, and 1.96–1.99 Å, respectively, from X-ray crystallography.[193] Clearly, the average VO bond length increases with V coordination number and the linear extrapolation to longer VO lengths leads to lower energy CT bands. Since the position of the λ_L band shifts the most, it has the largest effect on $\lambda_{CT,AVG}$ (see Table 3). Therefore, this equation is consistent with methods 1 and 2 (*i.e.*, λ_L *vs.* coordination number and E_g *vs.* V–O–V number or degree of polymerization). The selective resonance Raman enhancement of the V=O vibration at 220 nm demonstrates that this CT energy is associated with V=O. Extrapolation of the linear equation to shorter VO lengths indicates that λ_{CT} at 220 nm is correlated with a VO bond length of 1.61 Å, which is in agreement with the typical terminal V=O bond length of 1.58 Å obtained by EXAFS and theory.[29,202] Analogous to the value of $\lambda_{CT,AVG}$, the longest VO bond length has the most significant effect on $R_{VO,AVG}$ (see Table 3). Taken all together, the linear correlation is likely valid for each CT band position and for each VO bond length not just for average values.

Table 3 compares the predicted bond length obtained using the linear equation for each observed CT band position with the bond length from X-ray crystallography. It includes very short V=O lengths and much longer V–O lengths found in O_h reference compounds as well as intermediate V–O lengths found in T_d or O_h compounds. The agreement between predicted (R_{VO}) and measured bond lengths ($R_{VO,X\text{-}ray}$) is very good and covers a much wider range of VO bond lengths than Ronde's correlation.

Fig. 7 depicts the agreement between measured positions of the CT bands (λ_{CT}) corresponding to the measured VO bond lengths ($R_{VO,X\text{-}ray}$) and the linear equation obtained by fitting:

$$R_{VO,X\text{-}ray} = 1.199 + 0.00176\lambda_{CT}$$

In our view the major source of deviation (standard deviation = 0.04 Å) from the linear correlation is the experimental uncertainty of up to ±13 nm in determining the position of CT bands. See, for example, the variation in λ_{CT} positions obtained by different research groups for the same reference material in Table 3.

The linear equation can be considered to be a combination of two linear correlations: (1) between λ_{CT} and the totally-symmetric ν_1 VX (X = O, S, Se) frequency observed for tetrahedral oxo-, thio- and seleno-anions[203,204] and (2) between $R_{VO,X\text{-}ray}$ (including V=O) and the position of the highest-frequency VO (ν_1) Raman band.[193,205,206] Using this equation the VO bond lengths corresponding to each CT band position (short- or intermediate-, or long wavelength) can be estimated, and the number of distinguishable CT bands observed in UV-vis spectra sets a lower bound on the number of distinct VO bond lengths. This new assignment method for the UV-vis bands of vanadium oxides should be applicable (with a slightly different slope and intercept, or a simple polynomial equation) to the analogous molybdenum, niobium, and tungsten oxides based on a similar smooth correlation between the bond lengths and E_g or E_L or Raman M–O (ν_1) frequency.[193,201,207–209] An analysis that includes all of the CT bands in UV-vis spectra will provide more complete information on the coordination number (or degree of polymerization) and the surface structure for supported oxide species. One caveat that must be mentioned has to do with the common situation that supported oxide species exist as a coexisting mixture of types, *e.g.* monomer, oligomer, and partially hydroxylated species. Under this typical situation, the overlap

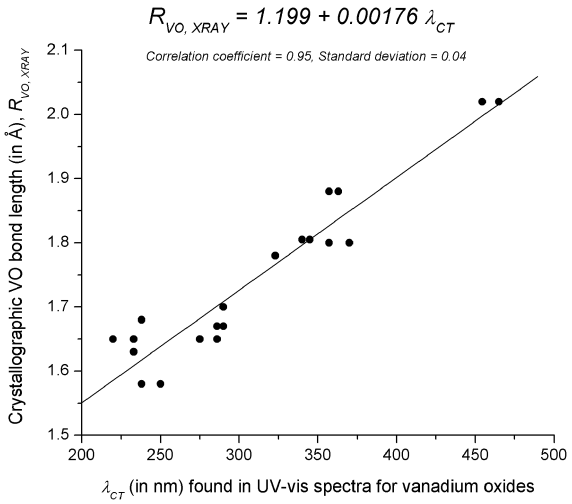

Fig. 7 A linear least-squares fit of λ_{CT} and $R_{VO,X\text{-}ray}$ data from Table 3. The intercept and slope (1.199 and 0.00176) of the linear fit are very similar to the values (1.224 and 0.00174) extracted from Ronde's data as shown in the main text.

of CT bands will be significant and it will be difficult to determine whether differing MO bond lengths are part of a single structure or pertain to different species.

It is interesting to compare the properties of V=O bonds in surface O=VO_3 species (T_d) and in crystalline V_2O_5 (O_h). The former structure can be found in (alumina-, silica-) supported vanadium oxides with low V loadings (<0.25 ML) and the latter with high V loadings or in bulk V_2O_5. The two types of V=O bonds have similar CT positions in their UV-vis spectra, but the overtone intensity is much weaker from bulk V_2O_5 in RR spectra excited at 220 nm. The weak overtone of V=O vibrations in V_2O_5 can be explained[1] by a very small displacement of the V=O bond length in the excited state, which suggests that V=O in V_2O_5 is not likely to be photoactive. In contrast, the strong overtone intensities produced by totally-symmetric V=O vibrations in surface O=VO_3 species (T_d) supported on alumina or silica signal a significant elongation of the V=O bond in the excited state, which suggests that V=O in the T_d structure should be photoactive. The conclusion inferred from RR results is in good agreement with the experimental observation that photocatalytic activity decreases at higher than 3.5 V wt% where bulk V_2O_5 starts to form.[184] This example shows that RR can be a useful spectroscopic probe of photocatalytic activity.

6.4 Information on structural change in the excited state: Jahn–Teller distortion

As described in Section 2, RR scattering involves a transition from the ground electronic state to an excited electronic state. Thus, RR experiments provide information about the nature of excited electronic state that is often unavailable from other spectroscopies. Examples include the bond length change, explained above, and Jahn–Teller (J–T) structural distortion in the excited electronic state.

In the resonance Raman spectra of supported vanadia excited at 287 nm, an enhanced band at $\sim$892 cm^{-1} was assigned to the non-totally-symmetric V–O stretching ν_4 (E) mode in C_{3v} symmetry or to the asymmetric ν_7 (A″) mode in C_s symmetry (see Fig. 1).[1] The ν_4 (E, C_{3v}) mode should be Jahn–Teller (J–T) active in C_{3v} symmetry in order for it to be enhanced *via* the A-term mechanism with an excited state having degenerate E symmetry.[1] The presence of J–T distortion in the excited electronic state indicated by RR results[1] is consistent with a recent DFT molecular orbital calculation for the C_{3v} structure of O=$V(OH)_3$ in the ground electronic state:[30]

(1) The e(3) mode in Table 2 and Fig. 2 of ref. 30 (equivalent to our ν_4 V–O stretching vibration) shows the strongest contribution to the J–T distortion.

(2) The totally-symmetric V=O stretching vibration, a_1(4) in Table 2 and Fig. 2 of ref. 30 and ν_1 (A_1) in our notation described in Fig. 1, couples to the excited electronic state, shows the second strongest contribution to the J–T distortion, but does not lower the molecular symmetry from C_{3v} to C_s.

The optimized structure in the (triplet) excited electronic state has C_s symmetry, and the J–T stabilization mainly comes from vibronic coupling of the E-symmetry LUMO and the E-symmetry vibrational mode.

These arguments are supported by another theoretical calculation[210] for O=$V(OSiH_3)_3$ which also finds a structural distortion and lowering of the symmetry from C_{3v} in the ground state to C_s in the excited electronic state.

6.5 Assignment of Raman bands: symmetric or not

Overtone and combination bands do not appear in normal, nonresonance Raman spectra, but frequently appear in resonance Raman (RR) spectra along with the enhanced fundamental bands. Overtones and combinations have been studied extensively in small molecules or ions[24,211] and biomolecules[37,212] by RR spectroscopy. In contrast, relatively few such studies exist in heterogeneous catalysts and catalysis. Examples include Mo=O and Mo–O vibrations on γ-Al_2O_3; V=O and V–O vibrations on θ-Al_2O_3 and on SiO_2 with 244 nm, 325 nm, 220 nm, and 287 nm excitation.[1,52,84]

The relationship between totally-symmetric and non-totally-symmetric modes and the appearance of overtones and combinations in the RR spectra has been described in the RR theory section and a recent article.[1] In brief, the clear appearance of overtone bands in addition to the enhanced fundamental bands is associated with totally-symmetric modes.[11,12] Since overtones of non-totally-symmetric modes generally do not appear, the presence of overtones is a clear marker for a totally-symmetric mode. Until now in the field of heterogeneous catalysts and catalysis, resonance enhanced fundamental bands have been the primary focus, but the additional information provided by the analysis of overtones is an important aid in assigning vibrational bands.

6.6 Information on molecular parameters

Overtone and combination bands observed in the RR spectra also provide useful information about molecular parameters such as the anharmonicity constant, dissociation energy, harmonic frequency, and anharmonic force constant. More details can be found in a recent article on vanadium oxide catalysts.[1]

The position and intensity of fundamental and overtone Raman bands determine both the harmonic wavenumber ω_e and anharmonicity constant $\omega_e x_e$ ($= x_{mm}$). ω_e ($= \omega_m$) is the vibrational wavenumber corrected for the anharmonicity of the potential. The anharmonicity constant is a measure of the deviation from the harmonic potential. $x_e = 0$ for the harmonic potential. The determination of both parameters makes it possible to estimate the dissociation limit (see below). The observed wavenumbers, $\nu_m(n)$, for fundamental ($n = 1$), 1st overtone ($n = 2$), and 2nd overtone ($n = 3$) from a polyatomic anharmonic oscillator are given[12,213] by the expression

$$\nu_m(n) = n\omega_m - n(n+1)x_{mm} + \cdots$$

where 'm' is normal mode identifier, *e.g.*, ω_1 and x_{11} for the ν_1 mode. A plot of $\nu_m(n)/n$ *versus* n should be a straight line, with slope x_{mm} and intercept $\omega_m - x_{mm}$ from which ω_m is derived. Typical plots for the overtone progressions in V=O and V–O are shown in published papers.[1,52]

The force constant can be used in many applications, *e.g.*, the correlation between the force constant and bond

length,[214,215] the relationship between force constant and activation energy[216] or dissociation energy, and the calculation of kinetic isotope effects in the catalytic reaction.[217] The anharmonicity-corrected force constant, f_e, or anharmonic force constant can be obtained using the diatomic oscillator approximation and the equation $\omega_e = (2\pi c)^{-1}(f_e/\mu)^{0.5}$ where μ is the reduced mass and ω_e is the harmonic wavenumber. f_e is, in theory, a more exact representation of the bond force constant than f obtained from the harmonic oscillator equation given by $\omega = (2\pi c)^{-1}(f/\mu)^{0.5}$ where ω is the wavenumber observed from IR or Raman spectra.[25,218,219] The force constants for V=O obtained from these equations are expected to be quite accurate because the V=O stretching mode (*e.g.*, in C_{3v} symmetry) involves no significant motion of the other atoms in the VO_4 unit.[25,220] The force constants for the V–O stretching mode will be less accurate because normal coordinate for V–O stretching includes movement of the V=O bond (see Fig. 1).[25] A more accurate estimate can be obtained using the 'effective' reduced mass μ_{eff} rather than the diatomic reduced mass of μ.[221]

The dissociation energy (D_0) along a normal coordinate represents the depth of the vibrational potential well below the dissociation limit (see Fig. 2). It can be calculated from the harmonic frequency, ω_m, and anharmonic constant, x_{mm}, using the standard equation for an anharmonic oscillator. By neglecting cubic and higher-order terms: D_0 (in cm^{-1}) = $0.25(\omega_m{}^2/x_{mm}) - 0.5\omega_m + 0.25x_{mm}$ where $0.5\omega_m - 0.25x_{mm}$ is the zero point energy.[220] The D_0 (kJ mol^{-1}) values for V=O and V–O modes determined from the RR spectra can be found in the literature.[1,52]

7. Surface-enhanced Raman spectroscopy (SERS)

SERS is a surface sensitive technique that involves very large enhancements in Raman scattering for species located at roughened metal surfaces, typically Au or Ag. This phenomenon was first recognized in 1977, when it was observed[222,223] that the Raman scattering intensity of pyridine adsorbed on electrochemically roughened Ag was enhanced by a factor of $\sim 10^6$. SERS quickly proved to be a powerful tool for fundamental studies of surface adsorbates. Advances in nanofabrication methods that produce substrates with controlled and well-defined plasmonic properties, along with improvements in laser sources, detection schemes, and theoretical modeling have led to the widespread application of SERS to diverse problems of chemical interest. Surface modification techniques have extended the applicability of SERS beyond coinage metal surfaces to many nanomaterials of catalytic interest. In addition, the ability to perform single molecule studies points to the exciting possibility of *in situ* vibrational characterization at single catalytic sites. *In situ* characterization of the binding and reaction of molecular adsorbates at catalytic interfaces constitutes a research area of enormous importance for the ultimate goal of rational catalyst design.

Many reviews on the fundamentals as well as applications of SERS exist in the literature;[224–228] the aim here is to highlight the virtues of SERS for the purpose of studying adsorbates at catalytically relevant interfaces. The advantages and challenges associated with such measurements as well as approaches to extend the applicability of SERS beyond coinage metal surfaces will be discussed.

7.1 Principles of SERS

Early on, significant research effort was aimed at achieving a mechanistic understanding of SERS. In the classical picture of Raman scattering, incident light induces a dipole moment in the molecule which in turn radiates at its oscillation frequencies. Since the induced dipole moment is a product of the molecular polarizability and the applied electric field, it follows that enhanced Raman scattering must arise from an increase in one of these two factors. SERS can therefore be understood as the product of a chemical and an electromagnetic effect.

The chemical mechanism is thought to be an enhancement in polarizability caused by direct interaction between the adsorbed molecule and the metal surface. Perturbations to the electronic structure of the molecule upon adsorption and charge-transfer effects result in an increase in the Raman cross-section for the adsorbed molecule relative to the solution phase. In general, however, the contribution to overall enhancement from chemical effects is quite modest (~ 10–10^2) in comparison to electromagnetic effects.

The electromagnetic mechanism is based on the interaction of light with the nanostructured metal surface, which excites an oscillation of the conduction electrons known as the localized surface plasmon resonance (LSPR). This resonance can occur in materials having a negative real and small positive imaginary dielectric constant, a condition that is met in the visible region for Au, Ag, and Cu. Excitation of the LSPR results in amplification of both the incident and scattered fields at the surface of the metal nanostructure, leading to very large enhancements in Raman scattering.

7.2 Fabricating SERS substrates: nanosphere lithography (NSL) method

A critical consideration in any SERS experiment is the choice of substrate. A multitude of nanostructured surfaces exist that give rise to enhanced scattering, including electrochemically roughened electrodes, metal island films, chemically synthesized nanoparticles, and arrays of nanostructures fabricated by lithographic techniques. Advances in nanofabrication have led to greater control over the size and shape, and therefore optical properties, of nanostructured features on a surface. In particular, nanosphere lithography (NSL) is a simple and effective method of reproducibly fabricating SERS substrates with tunable optical properties.[229] This technique involves self-assembly of polystyrene or silica nanospheres into a hexagonally close-packed array on a substrate. Metal deposition ($\sim$10–100 nm) over the sphere mask and subsequent removal of the spheres results in an ordered array of triangular nanoparticles. Alternatively, deposition of a thicker layer of metal ($\sim$200 nm) without removal of the sphere mask produces a metal film-over-nanospheres (FON) substrate. These NSL-fabricated substrates have typical enhancement factors of $\sim 10^7$. The frequency of the resonance position is controlled by varying the nanosphere diameter and

thickness of metal deposited. From a practical standpoint, the wavelength dependence of electromagnetic enhancement dictates that one should carefully choose the appropriate excitation wavelength and substrate LSPR in order to achieve maximum enhancement.[230] While triangular nanoparticle arrays have narrower and more tunable resonances, FON substrates have a much higher surface area for detection which is advantageous for sensing applications.

7.3 Thermally and chemically robust SERS substrates by Al_2O_3 coating for catalytic studies

One challenge in the use of SERS for catalytic studies has been the instability of SERS substrates under relevant reaction conditions. At elevated temperatures, for example, triangular Ag nanoparticles anneal into hemispheres, which exhibit relatively smaller electromagnetic enhancement.[231] The dependence of electromagnetic enhancement on the size and shape of nanoscale features underscores the importance of maintaining the structural integrity of SERS substrates. Thermally robust SERS substrates have been developed in which ultrathin Al_2O_3 overlayers deposited by atomic layer deposition (ALD) were used for stabilization.[232] Ag nanoparticles having just a 0.2–1.0 nm thick overlayer of Al_2O_3 were shown to be stable at temperatures up to 500 °C over several hours. Al_2O_3-coated Ag nanoparticles have also been shown to be stable against high power ultrafast laser pulses and therefore suitable as a platform for both linear and non-linear surface-enhanced laser spectroscopy.[233] In addition to thermal deformation, exposure to organic solvents or aqueous solution can also result in morphology changes to SERS substrates. Stability in various solvent environments, critical for liquid-phase studies, can also be achieved with the use of ultrathin Al_2O_3 overlayers. In the case of AgFONs, Al_2O_3 coatings as thin as 4 Å prevent surface oxidation and delamination of the Ag film upon exposure to water. Furthermore, Al_2O_3-coated AgFONs have demonstrated temporal stability up to 12 months.[234] For catalytic applications, therefore, the use of ALD to coat SERS substrates with ultrathin Al_2O_3 layers thus enables the study of surface adsorbates in liquid at elevated reaction temperatures using SERS.

An important consideration when modifying SERS substrates for catalytic studies is the distance dependence of SERS. Enhanced fields generated by excitation of the LSPR extend beyond the surface of the substrate, thereby creating a volume within several nanometres of the surface in which molecules can be detected. It has been shown that SERS intensity scales as r^{-10}:

$$I_{\mathrm{SERS}} = \left(\frac{a+r}{a}\right)^{-10}$$

where I_{SERS} is the intensity of a particular Raman mode, a is the average size of the field-enhancing features on the surface, and r is the distance from the enhancing surface to the adsorbate.[235] The distance dependence allows one to stabilize or functionalize a SERS substrate with materials of catalytic interest while utilizing the enhancing properties of the underlying substrate, but care must be taken to use ultrathin modifiers in order to minimize signal losses.

7.4 Functionalized SERS surfaces for catalysis: overlayer-SERS

A limiting factor in the widespread application of SERS to diverse systems of interest has been the restriction to Au, Ag, and Cu surfaces. While these metals are of great importance in heterogeneous catalysis, access to a wider range of catalytic materials is highly desirable and necessary for SERS to be a generally useful technique for catalytic studies. Toward this end, researchers have looked towards other plasmonic materials for SERS. Transition metals such as Pt, Pd, Rh, Ru, Fe, Co, and Ni have shown SERS activity,[236,237] although with much weaker enhancements than typically seen for Au and Ag. A different strategy is to functionalize a SERS-active substrate with the material of catalytic interest. In this case, sufficient coverage must be ensured to avoid interaction of adsorbate molecules with the underlying Au or Ag. In addition, due to the SERS distance dependence, the catalytic material must be sufficiently thin so as to be within the sensing range.

Weaver and co-workers extended the applicability of SERS to the study of catalytically interesting transition-metal interfaces using an overlayer approach.[238–241] Electrodeposition yielded ultrathin films (~3–5 monolayers thick) of catalytic metals (Pt, Pd, Ir, Rh, and Ru) over roughened Au electrodes. This "overlayer-SERS" strategy utilizes the electromagnetic enhancement from the underlying plasmonic material while providing a functionalized surface having different reactivity. Overlayer deposition enabled SERS studies of chemisorbate binding,[242,243] surface oxidation,[244] and catalytic reactions such as methanol oxidation,[245,246] on transition metal surfaces. Using a similar strategy, Au colloids immobilized on an ITO (indium tin oxide) electrode were coated with a monolayer of Pt or Pd using redox-replacement of underpotential-deposited Cu.[247] SERS measurements of CO and ethylene adsorption exhibited well-defined vibrational properties and pinhole-free coverage, demonstrating the potential of this technique for the preparation of diverse nanomaterials relevant to catalysis.

An alternative overlayer approach is the use of ALD to functionalize SERS-active substrates with materials of catalytic interest. ALD is a thin film growth technique based on the alternating use of self-terminating reactions between gaseous precursor molecules and a substrate.[248] The primary advantage of ALD over other deposition methods is the precise thickness control afforded by the self-limiting nature of the surface reactions. Film growth proceeds in a layer-by-layer fashion with atomic level control and is extremely uniform, even over high surface area and nanoporous structures. It is important to note that because SERS intensity falls off with increasing distance from the surface, the ability to grow films with subnanometre thickness is highly desirable to minimize signal losses. Moreover, the wide variety of materials that can be grown by ALD presents new possibilities for versatile surface functionalization. A wealth of metal oxides used in heterogeneous catalysis, such as Al_2O_3, TiO_2, and VO_x, are easily grown over SERS substrates by ALD. In addition, ALD has been shown to be an excellent technique for the synthesis of supported metal nanoparticles,[249–251] specifically Pd and Pt. Significantly, the use of ALD to grow both supported metal oxide and metal nanoparticle catalysts over SERS-active

substrates greatly extends the applicability of SERS to the study of surface adsorbates at catalytically relevant interfaces.

7.5 SERS: single-molecule detection sensitivity

To better understand the chemistry that occurs at a single active site within a heterogeneous catalyst, *in situ* techniques capable of single molecule detection are needed. Single-molecule fluorescence has been successfully applied to studies of single-nanoparticle catalysis, but this approach is restricted by the need for a fluorescent reaction product or fluorescent probe molecule.[252] Single-molecule SERS (SMSERS), which yields richer chemical information and is more broadly applicable, has the potential to overcome these limitations. Surface-enhanced Raman spectra from individual molecules were first observed in 1997 independently by the groups of Nie[253] and Kneipp.[254] Nie and Emory detected Raman scattering from single rhodamine 6G molecules adsorbed on Ag nanoparticles at concentrations corresponding to zero or one analyte molecule per nanoparticle ($<10^{-10}$ M). Kneipp *et al.* observed SMSERS of crystal violet on Ag nanoparticles in solution where fluctuations in signal intensity and statistical analysis were used as evidence of single-molecule behavior. In search of a more definitive proof of SMSERS, Etchegoin and co-workers introduced the bi-analyte technique which relied on competitive adsorption between two analytes, R6G and benzotriazole.[255] However, interpretation of results based on this approach can be difficult due to differences in Raman cross-section, absorption spectra, and surface binding affinity of the two analytes. The isotopologue approach developed by Dieringer *et al.* improves upon the bi-analyte technique by the use of two isotopologues which are chemically similar but have unique vibrational signatures.[256] At sufficiently low concentrations where only one molecule is adsorbed to a nanoparticle, SMSER spectra contain the features of only a single isotopologue. Recent efforts to elucidate the structure of SMSERS hot spots are directed toward the ultimate goal of developing tailored substrates with reproducible single-molecule activity.[257] Optimization of highly enhancing substrates will enable the general application of SMSERS and provide insight into many chemical problems, including those in heterogeneous catalysis.

7.6 SERS for liquid-phase heterogeneous catalysis: a comparison with ATR and SFG techniques

Reactions that occur at the solid/liquid interface are of great importance in many catalytic processes, for example in the processing of biomass to fuels. To characterize the binding and reaction of surface adsorbates, *in situ* techniques are needed that can identify surface species in aqueous solution. Attenuated Total Reflectance Infrared Spectroscopy (ATR-IR) has been used to study liquid-phase heterogeneous catalytic reactions,[258,259] but interference from strongly absorbing solvents, particularly water, can be problematic. The lack of surface specificity also makes data interpretation quite difficult as the spectra represent a mixture of species adsorbed on the surface of the catalyst as well as species dissolved in solution. Sum frequency generation (SFG) is a non-linear vibrational spectroscopy that can provide detailed information on the surface structure and orientation of molecules at buried interfaces. SFG studies of hydrocarbons at liquid/metal oxide interfaces point to the potential of this technique for *in situ* characterization of surface adsorbates in the liquid phase,[260] but SFG suffers from a limited spectral range. SERS, which provides detailed vibrational information over a wide spectral range, is ideally suited for measurements at the liquid/solid interface because of its superior surface sensitivity as well as its compatibility with water.

Using SERS, Heck *et al.* were able to study the catalytic hydrodechlorination of 1,1-dichloroethene (1,1-DCE) in water at room temperature.[261] In this work, Au nanoshells enhanced the catalytic activity of Pd islands while providing the surface-enhancement necessary for sensitive measurements. Adsorption and reaction of 1,1-DCE were monitored in real time with SERS, providing spectroscopic evidence for a number of surface intermediates in the reaction sequence. For many catalytic reactions of interest, one would also like the ability to measure SERS at the liquid/solid interface at elevated temperatures. As highlighted earlier, ultrathin metal oxide layers improve the thermal and solvent stability of Ag SERS substrates, thus enabling measurements under catalytically relevant conditions. To demonstrate that SERS is capable of observing surface adsorbates in a liquid environment at elevated temperatures, AgFON substrates optimized for operation with 532 nm laser excitation (nanosphere diameter = 390 nm and Ag film thickness = 200 nm) were functionalized with ultrathin layers of Al_2O_3 ($\sim$0.4 nm) using ALD. A 50 mM aqueous solution of pyridine was dosed over the surface in a flow cell held at various temperatures up to 90 °C and the SERS spectrum was measured (Fig. 8). This simple experiment demonstrates the potential of SERS as a tool for studying catalysis at the liquid/solid interface.

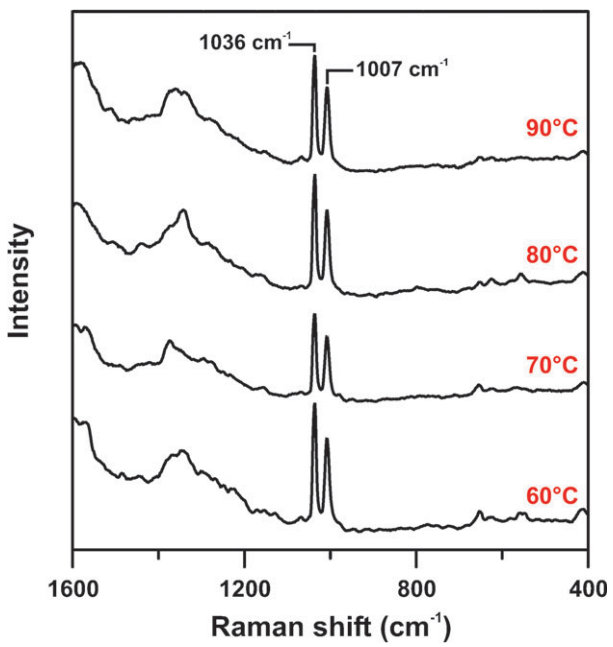

Fig. 8 Surface-enhanced Raman spectra of pyridine adsorbed on an Al_2O_3-modified AgFON in water at elevated temperatures. Strong peaks at 1036 and 1007 cm^{-1} are ring-breathing modes of pyridine.

8. Tip-enhanced Raman spectroscopy (TERS)

An important variation of SERS, tip-enhanced Raman spectroscopy (TERS), has emerged as a promising technique for *in situ* chemical analysis on the nanoscale. In TERS, enhancement arises from a metallic scanning probe microscopy (SPM) tip rather than from the substrate. By combining the sensitivity and rich chemical information of SERS with the excellent spatial resolution of scanning probe microscopy, TERS has the potential to be a very powerful tool for surface analysis. In this section, the advantages and challenges of this combined approach as well as advancements made in the application of TERS are outlined. The aim is to provide an overview of TERS and highlight its potential impact in the area of heterogeneous catalysis; for a more in-depth discussion of the technique, interested readers are referred to several reviews on the topic.[262–265]

When a Au or Ag SPM tip is irradiated with visible light, excitation of the LSPR results in an enhanced electromagnetic field which is locally confined around the tip apex. This enhanced electromagnetic field increases Raman scattering from molecules located in the near-field region of the tip by 3 to 6 orders of magnitude.[264] The use of an SPM tip also provides nanometre spatial resolution, a significant improvement to the diffraction-limited spatial resolution of SERS which is $\sim\lambda_{ex}/2$. The theoretical concept of TERS was first proposed in 1985 by Wessel, who imagined an optical probe with nanometre resolution based on spatial confinement of an electromagnetic field by surface plasmons of a metal particle.[266] The metal particle would enhance Raman scattering at the sample surface, and microscopy could be performed by raster scanning the particle across the surface. The experimental realization of such a technique was achieved with the first TERS measurements conducted fifteen years later.[267–269]

By bringing the enhancing feature (tip) to the sample, the restriction to coinage metal surfaces or the need for surface modification of SERS-active substrates is avoided. TERS has the potential to be a completely substrate general technique, an obvious advantage for the study of various catalytic surfaces. Combined spectral and topographical imaging capabilities provide both structural and chemical information about the composition of a surface. Importantly, TERS is a technique compatible with both ambient and ultra-high vacuum (UHV) environments. In UHV, integration of laser excitation with STM capabilities permits atomic resolution and structural elucidation of adsorbate molecules on clean, single-crystal or nanostructured surfaces in a controlled environment. TERS can therefore be a complementary characterization technique to the variety of other UHV analysis tools available such as EELS, XPS, TPD, *etc*. On the other hand, the ability to conduct TERS experiments under ambient conditions broadens the applicability of the technique and enables measurements under conditions relevant to various catalytic processes.

8.1 Experimental considerations of TERS

TERS is performed using either an atomic force microscope (AFM) or a scanning tunneling microscope (STM). An STM affords more control over the tip-sample gap, but is limited to analysis of conductive samples. An AFM can be used in either contact (tapping) or non-contact (shear-force) mode, depending on the application. When contact mode is used, it is extremely important to verify that analyte molecules did not attach to the tip upon contact. This can be done by measuring the Raman scattering from just the tip itself. Samples which may be damaged by contact or easily contaminate the tip are better examined using shear-force AFM where a safe distance between the tip and substrate is maintained. However, this distance can lead to lower signal owing to the distance dependence of the electromagnetic enhancement.

Two types of tips are commonly employed in TERS experiments: electrochemically etched Au or Ag wires, and AFM cantilevers metallized by vapor deposition. Perhaps the greatest challenge in TERS is the fabrication of robust, reproducible, highly-enhancing tips. With etched metal tips, the fragile apex can be easily damaged by contact; with metallized AFM tips, adhesion of the metal is often poor. While the optical properties of Ag may be more favorable in terms of enhancement, Ag is prone to oxidation and therefore Au tips are often used because of their superior chemical stability. Thin coatings of a metal oxide such as SiO_2 or Al_2O_3 have been shown to protect the tip from physical and chemical damage.[270,271] Tips are also susceptible to annealing and morphology changes caused by local heating which results from a very strong electromagnetic field at the tip. In addition to robustness, maintaining tip cleanliness is another issue of great importance in TERS studies. Several groups have found that highly enhancing tips often show intense signal from carbonaceous contamination.[272,273]

The experimental configuration needed for a TERS experiment is dictated primarily by the type of sample to be investigated. For opaque samples, the tip-sample junction can be illuminated from the side using a long working distance objective to focus and collect Raman scattered light. If the sample is transparent, an inverted microscope set-up can be used where in-line illumination is used and Raman scattered light is collected back through a high numerical aperture objective. In-line illumination can also be used with a parabolic mirror which focuses incident light on the tip-sample junction and collects a greater angle of scattered light. Perfect focusing of light on the tip sample junction and efficient collection of Raman scattered light are crucial to the success of TERS experiments. To avoid photodecomposition, it is usually necessary to keep laser power low ($\sim$a few mW) with short integration times.[263] Visible excitation is typically used since the plasmon resonances of Au and Ag are in this region, but TERS with near-UV excitation has recently been shown using an Al tip, albeit with much lower enhancement.[274]

Representative TER spectra obtained using a Au coated AFM tip under ambient conditions are shown in Fig. 9 (reprinted from ref. 275). In spectrum A, Raman scattering of benzenethiol adsorbed to an 8 nm Au island film (AuIF) is observed with high signal-to-noise when the tip is engaged in contact mode. In B, laser focus is maintained on the sample while the tip is withdrawn by 100 μm. When the AFM tip is re-engaged, the TER spectrum is reproduced (C). After several engage–disengage cycles, the sample was removed and Raman scattering form the tip itself was measured to ensure that benzenethiol molecules were not transferred from the

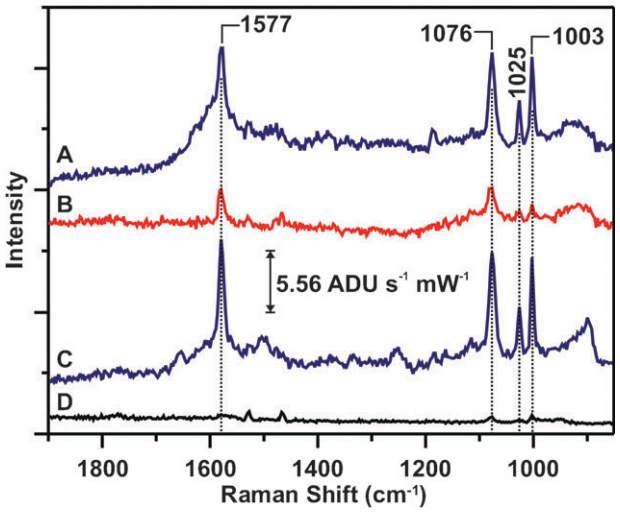

Fig. 9 Tip-enhanced Raman spectra for benzenethiol adsorbed to an 8 nm Au island film. (A) AFM tip engaged, (B) tip withdrawn by 100 μm, (C) tip re-engaged, (D) tip check. Reprinted from ref. 275.

substrate to the tip (D). The observed TERS signal therefore originated from the molecules adsorbed on the Au surface. By taking the difference in surface area between the laser spot ($\sim$1 μm^2) and the contact area of the AFM tip ($\sim$300 nm^2) into account, the average enhancement factor is estimated to be $>10^4$, demonstrating the sensitivity resulting from tip enhancement.

8.2 TERS measurements on single-crystalline surfaces

Surface science studies on single-crystalline samples have provided a wealth of information relevant to the understanding of heterogeneous catalysis. The use of Raman spectroscopy to probe surface adsorbates on flat single-crystals is extremely difficult owing to the weakness of Raman scattering and the lack of surface-enhancement, which requires nanoscale roughness. TERS overcomes this limitation and enables vibrational identification and characterization of surface adsorbed species on atomically smooth single-crystals. Pettinger *et al.* demonstrated TERS of adsorbed species on flame-annealed Au(111) and Pt(110) surfaces using a Au STM tip.[276] Raman enhancements on the order of 10^5 for CN^- ions adsorbed on Au(111) and 10^6 for malachite green isothiocyanate (MGITC) molecules on Au(111) were achieved. The detection of CN^- was notable because it was the first TERS measurement of a nonresonant species on a single-crystal surface. Ren *et al.* measured the TER spectrum of a self-assembled monolayer (SAM) of benzenethiol, another nonresonant molecule, on a flame-annealed Pt(110) surface.[277] Higher intensity was observed for benzenethiol adsorbed on Au(111) due to better optical coupling between the substrate and tip. Different vibrational frequencies and relative intensities were also observed on the two surfaces, highlighting the power of Raman spectroscopy to probe slight variations in adsorbate–substrate interaction.

8.3 Single-molecule detection sensitivity of TERS

The ability of TERS to reach single molecule detection sensitivity was first demonstrated by the groups of Raschke[278] and Pettinger,[279] who examined the dye molecules malachite green and malachite green isothiocyanate, respectively, adsorbed on Au surfaces. Subsequent measurements by the Zenobi group[280] of the dye molecule brilliant cresyl blue (BCB) on a Au film displayed behavior consistent with single molecule sensitivity. These initial single molecule studies, however, were based on indirect evidence such as spectral fluctuations. With TERS, the ability to image a single molecule in addition to collecting its Raman scattering spectrum offers an advantage in proving single molecule detection. Steidtner and Pettinger were able to image a single BCB molecule adsorbed on Au(111) using STM and subsequently collect its TER spectrum.[281] The key to this experiment was operation under UHV conditions where photobleaching was substantially reduced and thus a longer analysis time was possible. Additionally, they were able to perform TERS imaging of a single BCB molecule yielding chemical information with a lateral resolution of 15 nm. In this single molecule UHV-TERS experiment, enhancement of Raman scattering in the near-field of the STM tip was estimated to be $\sim 10^6$. Additional Raman enhancement resulting from resonant excitation of the dye molecule enabled single molecule detection sensitivity. These preliminary results in the area of single molecule TERS provide strong evidence for the possibility of using TERS to probe individual molecules at specific catalytic sites.

8.4 Applications of TERS and potential to heterogeneous catalysis

While experimental and theoretical effort is still primarily focused on understanding and improving TERS from a fundamental aspect, several groups are also working to extend the application of TERS to diverse problems in chemistry, biology, and materials science. Samples that have been investigated with TERS include biological molecules,[273,282–285] cells,[286,287] carbon nanotubes,[288–291] graphene,[292] polymer-blend thin films,[293,294] semiconductors,[295,296] and inorganic nanocrystals.[297,298]

The potential of TERS for *in situ* studies of relevance to heterogeneous catalysis is clearly illustrated in a recent study by Domke and Pettinger.[299] Using an ambient TERS set-up, both chemical and topographical information about the nature of cobalt *meso*-tetraphenylporphyrin (CoTPP) adsorbed on a Au(111) single crystal were obtained. STM images revealed spontaneous formation of two distinct surface phases: a well ordered adlayer of CoTPP molecules as well as a disordered phase. The corresponding TER spectrum from each region show chemically distinct signatures as well. The Raman fingerprint from the ordered phase resembles that of ligand-free CoTPP which is only weakly bound to the Au surface. The TER spectrum of the disordered phase, however, shows several additional vibrational bands which can be attributed to CO and/or NO axial binding to CoTPP. Simultaneous chemical and topographical discrimination between an axially complexed and ligand-free organometallic porphyrin on a single crystal surface demonstrates the power of TERS for the chemical analysis of surfaces.

Recently, the Zenobi group has advanced the application of TERS to studies at the liquid/solid interface.[265,300] In a proof-of-principal study, Schmid *et al*. performed TERS on a self-assembled monolayer (SAM) covered Au surface with both the tip and sample immersed in water.[300] The SiO_x/Ag-coated AFM tip was shown to be robust in an aqueous environment, and enhancements of $\sim 10^4$ were observed. Reduced carbon contamination for measurements in water as compared with measurements in air was also observed, indicating that a liquid environment may help to alleviate the problem of local heating and sample degradation. Performing TERS in a liquid environment enables *in situ* analysis of biological samples,[265] but this technique also opens the door for surface studies at the liquid/solid interface of importance for many heterogeneous catalytic processes.

9. Conclusions

An extensive explanation and discussion is provided of (1) several types of resonance Raman (RR) experimental systems, (2) three distinct sources of Raman (fluorescence) background, (3) structural changes in the excited state that are associated with the photocatalytic active site, (4) detection sensitivity comparison of RR with other commonly-used techniques, and (5) a new unified method to assign UV-vis bands compared with three well-known methods. RR is capable of (1) vibrational spectroscopic measurements in the whole spectral region ($\sim$100–4000 cm^{-1}) under *in situ*, high-temperature operando conditions, (2) high detection sensitivity and selectivity in probing surface metal oxides (as well as bulk species), and (3) providing useful information on photocatalytically-relevant excited states. These features make RR spectroscopy ideal for the characterization of solid catalysts and materials and catalytic reactions.

Surface specificity, single-molecule detection sensitivity, and compatibility with gaseous or liquid environments make SERS (surface-enhanced Raman spectroscopy) uniquely suited for obtaining detailed vibrational information on both catalysts and chemisorbates. Some limitations of instability of SERS substrates at high temperature and restriction to Au, Ag, and Cu surfaces can be overcome by the overlayer approach. Overlayer strategies such as ALD (atomic layer deposition) enable stabilization and functionalization of SERS substrates, therefore broadening the applicability of SERS to many systems of interest in heterogeneous catalysis. The powerful combination of SERS with scanning probe microscopy makes TERS (tip-enhanced Raman spectroscopy) a promising tool for achieving unprecedented structural and chemical characterization of catalytic surfaces. The progress highlighted in this review point to a promising future in which RR and enhanced Raman spectroscopy will have significant impact on the field of heterogeneous catalysis.

Acknowledgements

This work was supported by the Chemical Sciences, Geosciences and Biosciences Division, Office of Basic Energy Sciences, Office of Science, U.S. Department of Energy under Contract W-31-109-ENG-38 and Grant DE-FG02-03ER15457 and by the National Science Foundation through grant CHE-0911145.

References

1 H. S. Kim and P. C. Stair, *J. Phys. Chem. A*, 2009, **113**, 4346–4355.
2 H. Knozinger and G. Mestl, *Top. Catal.*, 1999, **8**, 45–55.
3 G. Mestl, *J. Mol. Catal. A: Chem.*, 2000, **158**, 45–65.
4 B. M. Weckhuysen and D. E. Keller, *Catal. Today*, 2003, **78**, 25–46.
5 Y. T. Chua and P. C. Stair, *J. Catal.*, 2000, **196**, 66–72.
6 P. C. Stair, *Adv. Catal.*, 2007, **51**, 75–98.
7 T. Nagasao and H. Yamada, *J. Raman Spectrosc.*, 1975, **3**, 153–160.
8 H. Yamada and Y. Yamamoto, *J. Chem. Soc., Faraday Trans. 1*, 1979, **75**, 1215–1221.
9 G. H. Smudde Jr and P. C. Stair, *Surf. Sci.*, 1994, **317**, 65–72.
10 G. Xiong, C. Li, Z. Feng, P. Ying, Q. Xin and J. Liu, *J. Catal.*, 1999, **186**, 234–237.
11 D. A. Long, *The Raman Effect: A Unified Treatment of the Theory of Raman Scattering by Molecules*, John Wiley & Sons, LTD, 2002.
12 R. J. H. Clark and B. Stewart, *Struct. Bonding*, 1979, **36**, 1–80.
13 B. Hudson, P. B. Kelly, L. D. Ziegler, R. A. Desiderio, D. P. Gerrity, W. Hess and R. Bates, *Adv. Laser Spectrosc.*, 1986, **3**, 1–32.
14 A. B. Myers, *Acc. Chem. Res.*, 1997, **30**, 519–527.
15 A. B. Myers, *Chem. Rev.*, 1996, **96**, 911–926.
16 A. M. Kelley, *J. Phys. Chem. A*, 2008, **112**, 11975–11991.
17 J. Neugebauer, *Phys. Rep.*, 2010, **489**, 1–87.
18 T. G. Spiro and P. Stein, *Annu. Rev. Phys. Chem.*, 1977, **28**, 501–521.
19 A. C. Albrecht, *J. Chem. Phys.*, 1961, **34**, 1476–1484.
20 A. C. Albrecht and M. C. Hutley, *J. Chem. Phys.*, 1971, **55**, 4438–4443.
21 J. Tang and A. C. Albrecht, in *Raman Spectroscopy*, ed. H. A. Szymanski, Plenum, New York, 1970, vol. 2, p. 33–68.
22 J. L. McHale, *Acc. Chem. Res.*, 2001, **34**, 265–272.
23 J. T. Hupp and R. D. Williams, *Acc. Chem. Res.*, 2001, **34**, 808–817.
24 R. J. H. Clark and T. J. Dines, *Angew. Chem., Int. Ed. Engl.*, 1986, **25**, 131–158.
25 K. Nakamoto, *Infrared and Raman spectra of inorganic and coordination compounds, Part A: Theory and applications in inorganic chemistry*, John Wiley & Sons Inc, New York, 5th edn, 1997.
26 Y. Nishimura, A. Y. Hirakawa and M. Tsuboi, in *Advances in Infrared and Raman Spectroscopy*, ed. R. J. H. Clark and R. E. Hester, Heyden & Son, London, 1978, vol. 5, pp. 217–275.
27 A. Y. Hirakawa and M. Tsuboi, *Science*, 1975, **188**, 359–361.
28 M. Tsuboi and A. Y. Hirakawa, *J. Raman Spectrosc.*, 1976, **5**, 75–86.
29 H. S. Kim, S. A. Zygmunt, P. C. Stair, P. Zapol and L. A. Curtiss, *J. Phys. Chem. C*, 2009, **113**, 8836–8843.
30 T. Sato, N. Iwahara, K. Tokunaga, K. Tanaka and T. Tanaka, *Top. Catal.*, 2009, **52**, 808–812.
31 E. J. Heller, *Acc. Chem. Res.*, 1981, **14**, 368–375.
32 E. J. Heller, R. L. Sundberg and D. Tannor, *J. Phys. Chem.*, 1982, **86**, 1822–1833.
33 S. Y. Lee and E. J. Heller, *J. Chem. Phys.*, 1979, **71**, 4777–4788.
34 Y. Y. Yang and J. I. Zink, *Inorg. Chem.*, 1985, **24**, 4012–4015.
35 S. K. Doorn and J. T. Hupp, *J. Am. Chem. Soc.*, 1989, **111**, 4704–4712.
36 K. A. Kane and L. Jensen, *J. Phys. Chem. C*, 2010, **114**, 5540–5546.
37 S. A. Asher, *Annu. Rev. Phys. Chem.*, 1988, **39**, 537–588.
38 T. G. Spiro and R. S. Czernuszewicz, in *Physical Methods in Bioinorganic Chemistry: Spectroscopy and Magnetism*, ed. L. Que, University Science Books, Sausalito, CA, 2000, pp. 59–120.
39 S. Bykov, I. Lednev, A. Ianoul, A. Mikhonin, C. Munro and S. A. Asher, *Appl. Spectrosc.*, 2005, **59**, 1541–1552.
40 X. J. Zhao, R. P. Chen, C. Tengroth and T. G. Spiro, *Appl. Spectrosc.*, 1999, **53**, 1200–1205.
41 S. A. Asher, R. J. Craig and M. James, *Rev. Sci. Instrum.*, 1983, **54**, 1657–1662.
42 S. P. A. Fodor, R. P. Rava, R. A. Copeland and T. G. Spiro, *J. Raman Spectrosc.*, 1986, **17**, 471–475.

43 L. D. Ziegler, *J. Chem. Phys.*, 1987, **86**, 1703–1714.
44 S. A. Asher, R. W. Bormett, X. G. Chen, D. H. Lemmon, N. Cho, P. Peterson, M. Arrigoni, L. Spinelli and J. Cannon, *Appl. Spectrosc.*, 1993, **47**, 628–633.
45 J. S. W. Holtz, R. W. Bormett, Z. H. Chi, N. J. Cho, X. G. Chen, V. Pajcini, S. A. Asher, L. Spinelli, P. Owen and M. Arrigoni, *Appl. Spectrosc.*, 1996, **50**, 1459–1468.
46 J. J. Kim, *Opt. Quantum Electron.*, 1991, **23**, S469–S476.
47 I. Calizo, I. Bejenari, M. Rahman, G. Liu and A. A. Balandin, *J. Appl. Phys.*, 2009, **106**, 043509.
48 D. C. Smith and G. Godard, *Spectrochim. Acta, Part A*, 2009, **73**, 428–435.
49 J. Zhang, M. J. Li, Z. C. Feng, J. Chen and C. Li, *J. Phys. Chem. B*, 2006, **110**, 927–935.
50 J. Zhang, Z. C. Feng, M. J. Li, J. Chen, Q. Xu, Y. X. Lian and C. Li, *Appl. Spectrosc.*, 2007, **61**, 38–47.
51 H. Tian, I. E. Wachs and L. E. Briand, *J. Phys. Chem. B*, 2005, **109**, 23491–23499.
52 Z. Wu, S. Dai and S. H. Overbury, *J. Phys. Chem. C*, 2010, **114**, 412–422.
53 C. Moisii, L. J. van de Burgt and A. E. Stiegman, *Chem. Mater.*, 2008, **20**, 3927–3935.
54 F. Fan, K. Sun, Z. Feng, H. Xia, B. Han, Y. Lian, P. Ying and C. Li, *Chem.–Eur. J.*, 2009, **15**, 3268–3276.
55 Y. Aki, M. Nagai, Y. Nagai, K. Imai, M. Aki, A. Sato, M. Kubo, S. Nagatomo and T. Kitagawa, *JBIC, J. Biol. Inorg. Chem.*, 2010, **15**, 147–158.
56 G. Balakrishnan, Y. Hu, S. B. Nielsen and T. G. Spiro, *Appl. Spectrosc.*, 2005, **59**, 776–781.
57 L. Sokolov and I. Mukerji, *J. Phys. Chem. B*, 1998, **102**, 8314–8319.
58 X. J. Zhao, C. Tengroth, R. P. Chen, W. R. Simpson and T. G. Spiro, *J. Raman Spectrosc.*, 1999, **30**, 773–776.
59 N. J. Everall, *Appl. Spectrosc.*, 2009, **63**, 245A–262A.
60 M. O. Guerrero-Perez and M. A. Banares, *Catal. Today*, 2006, **113**, 48–57.
61 G. Ricchiardi, A. Damin, S. Bordiga, C. Lamberti, G. Spano, F. Rivetti and A. Zecchina, *J. Am. Chem. Soc.*, 2001, **123**, 11409–11419.
62 E. U. Donev, R. Lopez, L. C. Feldman and R. F. Haglund, *Nano Lett.*, 2009, **9**, 702–706.
63 C. Krafft, B. Dietzek and J. Popp, *Analyst*, 2009, **134**, 1046–1057.
64 B. R. Wood, A. Hermelink, P. Lasch, K. R. Bambery, G. T. Webster, M. A. Khiavi, B. M. Cooke, S. Deed, D. Naumann and D. McNaughton, *Analyst*, 2009, **134**, 1119–1125.
65 V. Pajcini, C. H. Munro, R. W. Bormett, R. E. Witkowski and S. A. Asher, *Appl. Spectrosc.*, 1997, **51**, 81–86.
66 Z.-X. Gao, H.-S. Kim, Q. Sun, P. C. Stair and W. M. H. Sachtler, *J. Phys. Chem. B*, 2001, **105**, 6186–6190.
67 J. F. Haw, *In situ Spectroscopy in Heterogeneous Catalysis*, Wiley-VCH, Weinheim, 2002.
68 B. M. Weckhuysen, *Phys. Chem. Chem. Phys.*, 2003, **5**, 4351–4360.
69 M. A. Banares and G. Mestl, *Adv. Catal.*, 2009, **52**, 43–128.
70 H. Launay, S. Loridant, D. L. Nguyen, A. M. Volodin, J. L. Dubois and J. M. M. Millet, *Catal. Today*, 2007, **128**, 176–182.
71 G. Koyano, T. Saito and M. Misono, *Chem. Lett.*, 1997, 415–416.
72 E. L. Lee and I. E. Wachs, *J. Phys. Chem. C*, 2008, **112**, 6487–6498.
73 H. A. Ebrahim and E. Jamshidi, *Ind. Eng. Chem. Res.*, 2002, **41**, 2630–2636.
74 N. S. Grewal and S. C. Saxena, *Ind. Eng. Chem. Process Des. Dev.*, 1981, **20**, 108–116.
75 S. Xie, M. P. Rosynek and J. H. Lunsford, *Appl. Spectrosc.*, 1999, **53**, 1183–1187.
76 J. Li, G. Xiong, Z. Feng, Z. Liu, Q. Xin and C. Li, *Microporous Mesoporous Mater.*, 2000, **39**, 275–280.
77 V. S. Sullivan, S. D. Jackson and P. C. Stair, *J. Phys. Chem. B*, 2005, **109**, 352–356.
78 C. Zhang, P. M. Allotta, G. Xiong and P. C. Stair, *J. Phys. Chem. C*, 2008, **112**, 14501–14507.
79 K. D. Mielenz, *Appl. Opt.*, 1974, **13**, 2931–2933.
80 R. L. McCreery, *Raman Spectroscopy for Chemical Analysis*, John Wiley & Sons, Inc., 2000.
81 I. Ohana, Y. Yacoby and M. Bezalel, *Rev. Sci. Instrum.*, 1986, **57**, 9–12.
82 C. Julien, *J. Opt.*, 1980, **11**, 257–267.
83 V. Deckert, C. Fickert, D. Gernet, P. Vogt, T. Michelis and W. Kiefer, *Appl. Spectrosc.*, 1995, **49**, 253–255.
84 C. Li, *J. Catal.*, 2003, **216**, 203–212.
85 C. K. Johnson and R. Rubinovitz, *Spectrochim. Acta, Part A*, 1991, **47**, 1413–1421.
86 V. M. Hallmark, C. G. Zimba, J. D. Swalen and J. F. Rabolt, *Mikrochim. Acta*, 1988, **2**, 215–218.
87 R. Petry, M. Schmitt and J. Popp, *ChemPhysChem*, 2003, **4**, 14–30.
88 N. Everall, T. Hahn, P. Matousek, A. W. Parker and M. Towrie, *Appl. Spectrosc.*, 2001, **55**, 1701–1708.
89 W. Kiefer, *J. Raman Spectrosc.*, 2007, **38**, 1538–1553.
90 P. Matousek and N. Stone, *Analyst*, 2009, **134**, 1058–1066.
91 J. W. Ager, R. K. Nalla, K. L. Breeden and R. O. Ritchie, *J. Biomed. Opt.*, 2005, **10**, 034012-1–034012-8.
92 W. Kiefer, *J. Raman Spectrosc.*, 2008, **39**, 1710–1725.
93 G. Fevotte, *Chem. Eng. Res. Des.*, 2007, **85**, 906–920.
94 H. S. Sands, I. P. Hayward, T. E. Kirkbride, R. Bennett, R. J. Lacey and D. N. Batchelder, *J. Forensic Sci.*, 1998, **43**, 509–513.
95 P. J. Hendra, I. D. M. Turner, E. J. Loader and M. Stacey, *J. Phys. Chem.*, 1974, **78**, 300–304.
96 T. A. Egerton, A. H. Hardin, Y. Kozirovs and N. Sheppard, *J. Catal.*, 1974, **32**, 343–361.
97 W. B. Rippon, J. L. Koenig and A. G. Walton, *J. Agric. Food Chem.*, 1971, **19**, 692–697.
98 A. Dyan, P. Cenedese and P. Dubot, *J. Phys. Chem. B*, 2006, **110**, 10041–10050.
99 W. Hayes and A. M. Stoneham, *Defects and Defect Processes in Nonmetallic Solids*, John Wiley & Sons, New York, 1985.
100 J. H. Lunsford and J. P. Jayne, *J. Phys. Chem.*, 1966, **70**, 3464–3469.
101 H. Jeziorowski and H. Knözinger, *Chem. Phys. Lett.*, 1976, **42**, 162–165.
102 Q. Xing and G. Sasaki, *Solid State Ionics*, 2007, **178**, 179–185.
103 S. H. Cai, S. N. Rashkeev, S. T. Pantelides and K. Sohlberg, *Phys. Rev. Lett.*, 2002, **89**, 23550-1–23550-4.
104 R. L. Nelson and J. W. Hale, *Discuss. Faraday Soc.*, 1971, **52**, 77–88.
105 A. J. Tench and G. T. Pott, *Chem. Phys. Lett.*, 1974, **26**, 590–592.
106 W. Helfrich and F. R. Lipsett, *J. Chem. Phys.*, 1965, **43**, 4368–4376.
107 C. E. Nebel, *Nat. Photonics*, 2009, **3**, 564–566.
108 S. Stankic, J. Bernardi, O. Diwald and E. Knözinger, *J. Phys. Chem. B*, 2006, **110**, 13866–13871.
109 A. Splett, C. Splett and W. Pilz, *J. Raman Spectrosc.*, 1997, **28**, 481–485.
110 J. D. Levine and P. Mark, *Phys. Rev.*, 1966, **144**, 751–763.
111 C. Y. Ouyang, Z. Sljivancanin and A. Baldereschi, *Phys. Rev. B: Condens. Matter*, 2009, **79**, 235410-1–235410-7.
112 A. L. Shluger, K. P. McKenna, P. V. Sushko, D. M. Ramo and A. V. Kimmel, *Modell. Simul. Mater. Sci. Eng.*, 2009, **17**, 084004-1–084004-21.
113 P. E. Trevisanutto, P. V. Sushko, K. M. Beck, A. G. Joly, W. P. Hess and A. L. Shluger, *J. Phys. Chem. C*, 2009, **113**, 1274–1279.
114 J. Singh, N. Itoh, Y. Nakai, J. Kanasaki and A. Okano, *Phys. Rev. B: Condens. Matter*, 1994, **50**, 11730–11737.
115 M. Breysse, G. Coudurier, B. Claudel and L. Faure, *J. Lumin.*, 1982, **26**, 239–250.
116 K. H. Lee and J. H. Crawford, *Phys. Rev. B: Condens. Matter*, 1979, **19**, 3217–3221.
117 S. Ciraci and I. P. Batra, *Phys. Rev. B: Condens. Matter*, 1983, **28**, 982–992.
118 A. Stashans, E. Kotomin and J. L. Calais, *Phys. Rev. B: Condens. Matter*, 1994, **49**, 14854–14858.
119 J. R. Weber, A. Janotti and C. G. Van de Walle, *Microelectron. Eng.*, 2009, **86**, 1756–1759.
120 B. Shin, J. R. Weber, R. D. Long, P. K. Hurley, C. G. Van de Walle and P. C. McIntyre, *Appl. Phys. Lett.*, 2010, **96**, 152908.

121 D. Liu, S. J. Clark and J. Robertson, *Appl. Phys. Lett.*, 2010, **96**, 032905.
122 M. Muller, S. Stankic, O. Diwald, E. Knozinger, P. V. Sushko, P. E. Trevisanutto and A. L. Shluger, *J. Am. Chem. Soc.*, 2007, **129**, 12491–12496.
123 H. Werheit, *J. Phys.: Condens. Matter*, 2006, **18**, 10655–10662.
124 A. A. Sokol, S. A. French, S. T. Bromley, C. R. A. Catlow, H. J. J. v. Dam and P. Sherwood, *Faraday Discuss.*, 2007, **134**, 267–282.
125 N. Chestnoy, T. D. Harris, R. Hull and L. E. Brus, *J. Phys. Chem.*, 1986, **90**, 3393–3399.
126 B. Ealet, M. H. Elyakhloufi, E. Gillet and M. Ricci, *Thin Solid Films*, 1994, **250**, 92–100.
127 D. Renusch, M. Grimsditch, J. D. Jorgensen and J. P. Hodges, *Oxid. Met.*, 2001, **56**, 299–311.
128 A. N. Desikan, L. Huang and S. T. Oyama, *J. Chem. Soc., Faraday Trans.*, 1992, **88**, 3357–3365.
129 I. E. Wachs, *J. Catal.*, 1990, **124**, 570–573.
130 J. Z. Shyu, W. H. Weber and H. S. Gandhi, *J. Phys. Chem.*, 1988, **92**, 4964–4970.
131 I. E. Wachs, *Catal. Today*, 1996, **27**, 437–455.
132 M. A. Vuurman and I. E. Wachs, *J. Phys. Chem.*, 1992, **96**, 5008–5016.
133 D. Spielbauer, *Appl. Spectrosc.*, 1995, **49**, 650–654.
134 Z. L. Wu, H. S. Kim, P. C. Stair, S. Rugmini and S. D. Jackson, *J. Phys. Chem. B*, 2005, **109**, 2793–2800.
135 S. A. Asher, in *Handbook of Vibrational Spectroscopy*, ed. J. M. Chalmers and P. R. Griffiths, John Wiley & Sons Ltd, Chichester, 2002, vol. 1, pp. 557–571.
136 D. V. Martyshkin, R. C. Ahuja, A. Kudriavtsev and S. B. Mirov, *Rev. Sci. Instrum.*, 2004, **75**, 630–635.
137 T. Tahara and H.-O. Hamaguchi, *Appl. Spectrosc.*, 1993, **47**, 391–398.
138 A. Laubereau, D. von der Linde and W. Kaiser, *Phys. Rev. Lett.*, 1972, **28**, 1162–1165.
139 R. P. Van Duyne, D. L. Jeanmaire and D. F. Shriver, *Anal. Chem.*, 1974, **46**, 213–222.
140 J. B. Birks, *Photophysics of Aromatic Molecules*, John Wiley & Sons, London, New York, Sydney, Toronto, 1970.
141 P. Kukura, R. Frontiera and R. A. Mathies, *Phys. Rev. Lett.*, 2006, **96**, 238303-1–238303-4.
142 S. Y. Lee, D. H. Zhang, D. W. McCamant, P. Kukura and R. A. Mathies, *J. Chem. Phys.*, 2004, **121**, 3632–3642.
143 X. S. Xie, *239th ACS National Meeting*, San Francisco, CA, United States, 2010.
144 A. Mortensen, D. H. Christensen, O. F. Nielsen and E. Pedersen, *J. Raman Spectrosc.*, 1993, **24**, 667–673.
145 G. Careri, G. Signorel, M. Sampoli and V. Mazzacur, *J. Catal.*, 1972, **26**, 494–496.
146 J. P. Biscar and N. Kollias, *Chem. Phys. Lett.*, 1974, **24**, 563–564.
147 H. Jeziorowski and H. Knözinger, *Chem. Phys. Lett.*, 1977, **51**, 519–522.
148 R. Salzer, K.-H. Steinberg, P. Klaeboe and B. Schrader, *Zeolites*, 1991, **11**, 694–698.
149 Y. Y. Chen, J. Hyldtoft, C. J. H. Jacobsen and O. F. Nielsen, *Spectrochim. Acta, Part A*, 1995, **51**, 2161–2169.
150 P. L. J. Gunter, J. W. Niemantsverdriet, F. H. Ribeiro and G. A. Somorjai, *Catal. Rev. Sci. Eng.*, 1997, **39**, 77–168.
151 D. I. Ostrovskii, A. M. Yaremko and I. P. Vorona, *J. Raman Spectrosc.*, 1997, **28**, 771–778.
152 N. A. Atamas, A. M. Yaremko, L. A. Bulavin, V. E. Pogorelov, S. Berski, Z. Latajka, H. Ratajczak and A. Abkowicz-Bienko, *J. Mol. Struct.*, 2002, **605**, 187–198.
153 H. Ratajczak and A. M. Yaremko, *Chem. Phys. Lett.*, 1995, **243**, 348–353.
154 H. Ratajczak, A. J. Barnes, J. Baran, A. M. Yaremko, Z. Latajka and P. Dopleralski, *J. Mol. Struct.*, 2008, **887**, 9–19.
155 A. Kudelski, *Talanta*, 2008, **76**, 1–8.
156 S. A. Asher, *Anal. Chem.*, 1984, **56**, 720–724.
157 A. Ianoul, T. Coleman and S. A. Asher, *Anal. Chem.*, 2002, **74**, 1458–1461.
158 A. Campion, J. K. Brown and V. M. Grizzle, *Surf. Sci.*, 1982, **115**, L153–L158.
159 M. Valden, S. Pak, X. Lai and D. W. Goodman, *Catal. Lett.*, 1998, **56**, 7–10.
160 S. L. Wegener, H. S. Kim, T. J. Marks, P. C. Stair, *239th ACS National Meeting*, San Francisco, CA, United States, 2010.
161 S. R. Bare and T. Ressler, *Adv. Catal.*, 2009, **52**, 339–465.
162 C. Hess, M. Bonn, S. Funk and M. Wolf, *Chem. Phys. Lett.*, 2000, **325**, 139–145.
163 F. Gao, Y. Wang, Y. Cai and D. W. Goodman, *J. Phys. Chem. C*, 2009, **113**, 174–181.
164 S. Boujday, C. Y. Gu, M. Girardot, M. Salmain and C. M. Pradier, *Talanta*, 2009, **78**, 165–170.
165 J. Bollmann, T. Leisegang, D. C. Meyer, J. Weber and H. E. Mahnke, *Physica B (Amsterdam)*, 2006, **376**, 57–60.
166 Y. R. Shen, *Nature*, 1989, **337**, 519–525.
167 G. Rupprechter, *Adv. Catal.*, 2007, **51**, 133–263.
168 S. Roke, W. G. Roeterdink, J. E. G. J. Wijnhoven, A. V. Petukhov, A. W. Kleyn and M. Bonn, *Phys. Rev. Lett.*, 2003, **91**, 258302.
169 I. V. Stiopkin, H. D. Jayathilake, A. N. Bordenyuk and A. V. Benderskii, *J. Am. Chem. Soc.*, 2008, **130**, 2271.
170 D. M. Meier, A. Urakawa and A. Baiker, *Analyst*, 2009, **134**, 1779–1780.
171 E. V. Efremov, F. Ariese and C. Gooijer, *Anal. Chim. Acta*, 2008, **606**, 119–134.
172 S. A. Asher, *Anal. Chem.*, 1993, **65**, A59–A66.
173 R. S. Czernuszewicz, J. Legall, I. Moura and T. G. Spiro, *Inorg. Chem.*, 1986, **25**, 696–700.
174 T. C. Strekas, A. J. Packer and T. G. Spiro, *J. Raman Spectrosc.*, 1973, **1**, 197–206.
175 R. J. Sension, R. J. Brudzynski and B. S. Hudson, *Phys. Rev. Lett.*, 1988, **61**, 694–697.
176 F. Amano and T. Tanaka, *Chem. Lett.*, 2006, 468–473.
177 M. Anpo and M. Che, *Adv. Catal.*, 1999, **44**, 119–257.
178 M. Anpo, S. Dzwigaj and M. Che, *Adv. Catal.*, 2009, **52**, 1–42.
179 M. Anpo, I. Tanahashi and Y. Kubokawa, *J. Phys. Chem.*, 1980, **84**, 3440–3443.
180 A. M. Gritscov, V. A. Shvets and V. B. Kazansky, *Chem. Phys. Lett.*, 1975, **35**, 511–512.
181 M. Iwamoto, H. Furukawa, K. Matsukami, T. Takenaka and S. Kagawa, *J. Am. Chem. Soc.*, 1983, **105**, 3719–3720.
182 H. H. Patterson, J. Cheng, S. Despres, M. Sunamoto and M. Anpo, *J. Phys. Chem.*, 1991, **95**, 8813–8818.
183 K. Teramura, T. Hosokawa, T. Ohuchi, T. Shishido and T. Tanaka, *Chem. Phys. Lett.*, 2008, **460**, 478–481.
184 K. Teramura, T. Ohuchi, T. Shishido and T. Tanaka, *J. Phys. Chem. C*, 2009, **113**, 17018–17024.
185 F. C. Jentoft, in *Advances in Catalysis*, Elsevier Academic Press Inc, San Diego, 2009, vol. 52, pp. 129–211.
186 T. Petrenko and F. Neese, *J. Chem. Phys.*, 2007, **127**, 164319-1–164319-15.
187 N. Moussa and A. Ghorbel, *Appl. Surf. Sci.*, 2008, **255**, 2270–2275.
188 A. B. P. Lever, *Inorganic Electronic Spectroscopy*, Elsevier, Amsterdam, Oxford, New York, Tokyo, 2nd edn, 1984.
189 M. Schraml-Marth, A. Wokaun, M. Pohl and H. L. Krauss, *J. Chem. Soc., Faraday Trans.*, 1991, **87**, 2635–2646.
190 T. Tanaka, Y. Nishimura, S. Kawasaki, M. Ooe, T. Funabiki and S. Yoshida, *J. Catal.*, 1989, **118**, 327–338.
191 L.-X. Dai, K. Tabata, E. Suzuki and T. Tatsumi, *Chem. Mater.*, 2001, **13**, 208–212.
192 G. Centi, S. Perathoner, F. Trifiro, A. Aboukais, C. F. Aissi and M. Guelton, *J. Phys. Chem.*, 1992, **96**, 2617–2629.
193 F. D. Hardcastle and I. E. Wachs, *J. Phys. Chem.*, 1991, **95**, 5031–5041.
194 R. Enjalbert and J. Galy, *Acta Crystallogr., Sect. C: Cryst. Struct. Commun.*, 1986, **42**, 1467–1469.
195 X. T. Gao and I. E. Wachs, *J. Phys. Chem. B*, 2000, **104**, 1261–1268.
196 A. M. d. A. Cruz and J. Guillaume Eon, *Appl. Catal., A*, 1998, **167**, 203–213.
197 Y. M. Liu, S. H. Xie, Y. Cao, H. Y. He and K. N. Fan, *J. Phys. Chem. C*, 2010, **114**, 5941–5946.
198 F. Arena, F. Frusteri, G. Martra, S. Coluccia and A. Parmaliana, *J. Chem. Soc., Faraday Trans.*, 1997, **93**, 3849–3854.
199 G. Busca, G. Centi, L. Marchetti and F. Trifiro, *Langmuir*, 1986, **2**, 568–577.

200 H. Ronde and J. G. Snijders, *Chem. Phys. Lett.*, 1977, **50**, 282–283.
201 H. So and M. T. Pope, *Inorg. Chem.*, 1972, **11**, 1441–1443.
202 D. E. Keller, F. M. F. de Groot, D. C. Koningsberger and B. M. Weckhuysen, *J. Phys. Chem. B*, 2005, **109**, 10223–10233.
203 R. Kebabcioglu, A. Müller and W. Rittner, *J. Mol. Struct.*, 1971, **9**, 207–211.
204 R. Kebabcioglu and A. Müller, *Chem. Phys. Lett.*, 1971, **8**, 59–62.
205 K. R. Asmis, G. Meijer, M. Bruemmer, C. Kaposta, G. Santambrogio, L. Woeste and J. Sauer, *J. Chem. Phys.*, 2004, **120**, 6461–6470.
206 V. Brazdova, M. V. Ganduglia-Pirovano and J. Sauer, *J. Phys. Chem. B*, 2005, **109**, 394–400.
207 F. D. Hardcastle and I. E. Wachs, *J. Raman Spectrosc.*, 1990, **21**, 683–691.
208 F. D. Hardcastle and I. E. Wachs, *J. Raman Spectrosc.*, 1995, **26**, 397–405.
209 R. S. Weber, *J. Catal.*, 1995, **151**, 470–474.
210 M. Krauss, *THEOCHEM*, 1999, **458**, 73–79.
211 W. Kiefer, *Appl. Spectrosc.*, 1974, **28**, 115–134.
212 T. G. Spiro and R. S. Czernuszewicz, in *Physical Methods in Bioinorganic Chemistry: Spectroscopy and Magnetism*, ed. L. Que, University Science Books, 2000.
213 R. J. H. Clark, in *Advances in Infrared and Raman Spectroscopy*, ed. R. J. H. Clark and R. E. Hester, Heyden & Son Ltd, 1975, vol. 1, pp. 143–172.
214 R. M. Badger, *J. Chem. Phys.*, 1934, **2**, 128–131.
215 F. A. Cotton and R. M. Wing, *Inorg. Chem.*, 1965, **4**, 867–873.
216 E. T. Denisov and I. B. Afanas'ev, *Oxidation and Antioxidants in Organic Chemistry and Biology*, CRC Press, 2005.
217 I. Kobal, U. Burghaus, M. Senegacnik and N. Ogrinc, *J. Phys. Chem. B*, 1998, **102**, 6787–6791.
218 G. Herzberg, *Spectra of Diatomic Molecules*, D. van Nostrand company, Inc, New York, 2nd edn, 1950.
219 D. C. Harris and M. D. Bertolucci, *Symmetry and Spectroscopy: An Introduction to Vibrational and Electronic Spectroscopy*, Dover Publications, Inc., New York, 1978.
220 G. Herzberg, *Infrared and Raman Spectra of Polyatomic Molecules*, D. van Nostrand company, Inc, New York, 1945.
221 S. Dong, R. Padmakumar, R. Banerjee and T. G. Spiro, *Inorg. Chim. Acta*, 1998, **270**, 392–398.
222 M. G. Albrecht and J. A. Creighton, *J. Am. Chem. Soc.*, 1977, **99**, 5215–5217.
223 D. L. Jeanmaire and R. P. Van Duyne, *J. Electroanal. Chem.*, 1977, **84**, 1–20.
224 A. Campion and P. Kambhampati, *Chem. Soc. Rev.*, 1998, **27**, 241–250.
225 E. C. Le Ru and P. G. Etchegoin, *Principles of Surface-enhanced Raman Spectroscopy and Related Plasmonic Effects*, Elsevier, Amsterdam, 1st edn, 2009.
226 M. Moskovits, *Rev. Mod. Phys.*, 1985, **57**, 783–826.
227 A. Otto, I. Mrozek, H. Grabhorn and W. Akemann, *J. Phys.: Condens. Matter*, 1992, **4**, 1143–1212.
228 P. L. Stiles, J. A. Dieringer, N. C. Shah and R. P. Van Duyne, *Annu. Rev. Anal. Chem.*, 2008, **1**, 601–626.
229 C. L. Haynes and R. P. Van Duyne, *J. Phys. Chem. B*, 2001, **105**, 5599–5611.
230 A. D. McFarland, M. A. Young, J. A. Dieringer and R. P. Van Duyne, *J. Phys. Chem. B*, 2005, **109**, 11279–11285.
231 A. J. Haes, C. L. Haynes, A. D. McFarland, G. C. Schatz, R. R. Van Duyne and S. L. Zou, *MRS Bull.*, 2005, **30**, 368–375.
232 A. V. Whitney, J. W. Elam, P. C. Stair and R. P. Van Duyne, *J. Phys. Chem. C*, 2007, **111**, 16827–16832.
233 J. Sung, K. M. Kosuda, J. Zhao, J. W. Elam, K. G. Spears and R. P. Van Duyne, *J. Phys. Chem. C*, 2008, **112**, 5707–5714.
234 X. Y. Zhang, J. Zhao, A. V. Whitney, J. W. Elam and R. P. Van Duyne, *J. Am. Chem. Soc.*, 2006, **128**, 10304–10309.
235 B. J. Kennedy, S. Spaeth, M. Dickey and K. T. Carron, *J. Phys. Chem. B*, 1999, **103**, 3640–3646.
236 M. E. Abdelsalam, S. Mahajan, P. N. Bartlett, J. J. Baumberg and A. E. Russell, *J. Am. Chem. Soc.*, 2007, **129**, 7399–7406.
237 Z. Q. Tian, B. Ren and D. Y. Wu, *J. Phys. Chem. B*, 2002, **106**, 9463–9483.
238 M. J. Weaver, *Top. Catal.*, 1999, **8**, 65–73.
239 M. J. Weaver, *J. Raman Spectrosc.*, 2002, **33**, 309–317.
240 M. J. Weaver, S. Z. Zou and H. Y. H. Chan, *Anal. Chem.*, 2000, **72**, 38A–47A.
241 S. Z. Zou, C. T. Williams, E. K. Y. Chen and M. J. Weaver, *J. Am. Chem. Soc.*, 1998, **120**, 3811–3812.
242 H. Luo and M. J. Weaver, *Langmuir*, 1999, **15**, 8743–8749.
243 S. Z. Zou, C. T. Williams, E. K. Y. Chen and M. J. Weaver, *J. Phys. Chem. B*, 1998, **102**, 9039–9049.
244 S. Z. Zou, H. Y. H. Chan, C. T. Williams and M. J. Weaver, *Langmuir*, 2000, **16**, 754–763.
245 H. Y. H. Chan, C. T. Williams, M. J. Weaver and C. G. Takoudis, *J. Catal.*, 1998, **174**, 191–200.
246 C. T. Williams, C. G. Takoudis and M. J. Weaver, *J. Phys. Chem. B*, 1998, **102**, 406–416.
247 S. Park, P. X. Yang, P. Corredor and M. J. Weaver, *J. Am. Chem. Soc.*, 2002, **124**, 2428–2429.
248 M. Ritala and M. Leskela, in *Handbook of Thin Film Materials*, ed. H. S. Naiwa, Academic, San Diego, 2002, vol. 1, pp. 103–159.
249 S. T. Christensen, J. W. Elam, F. A. Rabuffetti, Q. Ma, S. J. Weigand, B. Lee, S. Seifert, P. C. Stair, K. R. Poeppelmeier, M. C. Hersam and M. J. Bedzyk, *Small*, 2009, **5**, 750–757.
250 H. Feng, J. W. Elam, J. A. Libera, W. Setthapun and P. C. Stair, *Chem. Mater.*, 2010, **22**, 3133–3142.
251 J. L. Lu and P. C. Stair, *Angew. Chem., Int. Ed.*, 2010, **49**, 2547–2551.
252 P. Chen, W. Xu, X. Zhou, D. Panda and A. Kalininskiy, *Chem. Phys. Lett.*, 2009, **470**, 151–157.
253 S. M. Nie and S. R. Emory, *Science*, 1997, **275**, 1102–1106.
254 K. Kneipp, Y. Wang, H. Kneipp, L. T. Perelman, I. Itzkan, R. Dasari and M. S. Feld, *Phys. Rev. Lett.*, 1997, **78**, 1667–1670.
255 E. C. Le Ru, M. Meyer and P. G. Etchegoin, *J. Phys. Chem. B*, 2006, **110**, 1944–1948.
256 J. A. Dieringer, R. B. Lettan, K. A. Scheidt and R. P. Van Duyne, *J. Am. Chem. Soc.*, 2007, **129**, 16249–16256.
257 J. P. Camden, J. A. Dieringer, Y. M. Wang, D. J. Masiello, L. D. Marks, G. C. Schatz and R. P. Van Duyne, *J. Am. Chem. Soc.*, 2008, **130**, 12616–12617.
258 T. Burgi and A. Baiker, in *Advances in Catalysis*, Elsevier Academic Press Inc, San Diego, 2006, vol. 50, pp. 227–283.
259 D. Ferri and A. Baiker, *Top. Catal.*, 2009, **52**, 1323–1333.
260 A. M. Buchbinder, E. Weitz and F. M. Geiger, *J. Phys. Chem. C*, 2010, **114**, 554–566.
261 K. N. Heck, B. G. Janesko, G. E. Scuseria, N. J. Halas and M. S. Wong, *J. Am. Chem. Soc.*, 2008, **130**, 16592–16600.
262 E. Bailo and V. Deckert, *Chem. Soc. Rev.*, 2008, **37**, 921–930.
263 K. F. Domke and B. Pettinger, *ChemPhysChem*, 2010, **11**, 1365–1373.
264 B. Pettinger, in *Surface-Enhanced Raman Scattering: Physics and Applications*, Springer-Verlag, 2006, vol. 103, pp. 217–240.
265 B. S. Yeo, J. Stadler, T. Schmid, R. Zenobi and W. H. Zhang, *Chem. Phys. Lett.*, 2009, **472**, 1–13.
266 J. Wessel, *J. Opt. Soc. Am. B*, 1985, **2**, 1538–1541.
267 M. S. Anderson, *Appl. Phys. Lett.*, 2000, **76**, 3130–3132.
268 N. Hayazawa, Y. Inouye, Z. Sekkat and S. Kawata, *Opt. Commun.*, 2000, **183**, 333–336.
269 R. M. Stockle, Y. D. Suh, V. Deckert and R. Zenobi, *Chem. Phys. Lett.*, 2000, **318**, 131–136.
270 C. A. Barrios, A. V. Malkovskiy, A. M. Kisliuk, A. P. Sokolov and M. D. Foster, *J. Phys. Chem. C*, 2009, **113**, 8158–8161.
271 X. D. Cui, D. Erni, W. H. Zhang and R. Zenobi, *Chem. Phys. Lett.*, 2008, **453**, 262–265.
272 M. Chaigneau, G. Picardi and R. Ossikovski, *Surf. Sci.*, 2010, **604**, 701–705.
273 K. F. Domke, D. Zhang and B. Pettinger, *J. Am. Chem. Soc.*, 2007, **129**, 6708–6709.
274 V. Poborchii, T. Tada, T. Kanayama and P. Geshev, *J. Raman Spectrosc.*, 2009, **40**, 1377–1385.
275 J. A. Dieringer, A. D. McFarland, N. C. Shah, D. A. Stuart, A. V. Whitney, C. R. Yonzon, M. A. Young, X. Y. Zhang and R. P. Van Duyne, *Faraday Discuss.*, 2006, **132**, 9–26.
276 B. Pettinger, B. Ren, G. Picardi, R. Schuster and G. Ertl, *Phys. Rev. Lett.*, 2004, **92**, 096101.
277 B. Ren, G. Picardi, B. Pettinger, R. Schuster and G. Ertl, *Angew. Chem., Int. Ed.*, 2005, **44**, 139–142.

278 C. C. Neacsu, J. Dreyer, N. Behr and M. B. Raschke, *Phys. Rev. B: Condens. Matter Mater. Phys.*, 2006, **73**, 193406.
279 K. F. Domke, D. Zhang and B. Pettinger, *J. Am. Chem. Soc.*, 2006, **128**, 14721–14727.
280 W. H. Zhang, B. S. Yeo, T. Schmid and R. Zenobi, *J. Phys. Chem. C*, 2007, **111**, 1733–1738.
281 J. Steidtner and B. Pettinger, *Phys. Rev. Lett.*, 2008, **100**, 236101.
282 E. Bailo and V. Deckert, *Angew. Chem., Int. Ed.*, 2008, **47**, 1658–1661.
283 T. Deckert-Gaudig, E. Bailo and V. Deckert, *Phys. Chem. Chem. Phys.*, 2009, **11**, 7360–7362.
284 B. S. Yeo, S. Madler, T. Schmid, W. H. Zhang and R. Zenobi, *J. Phys. Chem. C*, 2008, **112**, 4867–4873.
285 D. Zhang, K. F. Domke and B. Pettinger, *ChemPhysChem*, 2010, **11**, 1662–1665.
286 U. Neugebauer, P. Rosch, M. Schmitt, J. Popp, C. Julien, A. Rasmussen, C. Budich and V. Deckert, *ChemPhysChem*, 2006, **7**, 1428–1430.
287 U. Neugebauer, U. Schmid, K. Baumann, W. Ziebuhr, S. Kozitskaya, V. Deckert, M. Schmitt and J. Popp, *ChemPhysChem*, 2007, **8**, 124–137.
288 L. G. Cancado, A. Hartschuh and L. Novotny, *J. Raman Spectrosc.*, 2009, **40**, 1420–1426.
289 A. Hartschuh, E. J. Sanchez, X. S. Xie and L. Novotny, *Phys. Rev. Lett.*, 2003, **90**, 095503.
290 N. Hayazawa, T. Yano, H. Watanabe, Y. Inouye and S. Kawata, *Chem. Phys. Lett.*, 2003, **376**, 174–180.
291 Y. Saito, N. Hayazawa, H. Kataura, T. Murakami, K. Tsukagoshi, Y. Inouye and S. Kawata, *Chem. Phys. Lett.*, 2005, **410**, 136–141.
292 Y. Saito, P. Verma, K. Masui, Y. Inouye and S. Kawata, *J. Raman Spectrosc.*, 2009, **40**, 1434–1440.
293 X. Wang, D. Zhang, K. Braun, H. J. Egelhaaf, C. J. Brabec and A. J. Meixner, *Adv. Funct. Mater.*, 2010, **20**, 492–499.
294 B. S. Yeo, E. Amstad, T. Schmid, J. Stadler and R. Zenobi, *Small*, 2009, **5**, 952–960.
295 K. F. Domke and B. Pettinger, *J. Raman Spectrosc.*, 2009, **40**, 1427–1433.
296 N. Marquestaut, D. Talaga, L. Servant, P. Yang, P. Pauzauskie and F. Lagugné-Labarthet, *J. Raman Spectrosc.*, 2009, **40**, 1441–1445.
297 S. Berweger, C. C. Neacsu, Y. B. Mao, H. J. Zhou, S. S. Wong and M. B. Raschke, *Nat. Nanotechnol.*, 2009, **4**, 496–499.
298 S. Berweger and M. B. Raschke, *J. Raman Spectrosc.*, 2009, **40**, 1413–1419.
299 K. F. Domke and B. Pettinger, *ChemPhysChem*, 2009, **10**, 1794–1798.
300 T. Schmid, B. S. Yeo, G. Leong, J. Stadler and R. Zenobi, *J. Raman Spectrosc.*, 2009, **40**, 1392–1399.